

Determination of the charge carrier density in organic solar cells: A tutorial

Cite as: J. Appl. Phys. **131**, 221101 (2022); doi: [10.1063/5.0094955](https://doi.org/10.1063/5.0094955)

Submitted: 7 April 2022 · Accepted: 11 May 2022 ·

Published Online: 9 June 2022



Joachim Vollbrecht,^{1,2,a)}  Nurlan Tokmoldin,^{1,b)}  Bowen Sun,¹  Viktor V. Brus,³  Safa Shoaee,^{1,c)} 
and Dieter Neher^{2,d)} 

AFFILIATIONS

¹Disordered Semiconductor Optoelectronics, Institute of Physics and Astronomy, University of Potsdam, Karl-Liebknecht-Straße 24–25, 14476 Potsdam-Golm, Germany

²Soft Matter Physics and Optoelectronics, Institute of Physics and Astronomy, University of Potsdam, Karl-Liebknecht-Straße 24–25, 14476 Potsdam-Golm, Germany

³Department of Physics, School of Sciences and Humanities, Nazarbayev University, Nur-Sultan 010000, Kazakhstan

^{a)}**Current address:** Institut für Solarenergieforschung GmbH, Am Ohrberg 1, 31860 Emmerthal, Germany.

Electronic mail: vollbrecht@uni-potsdam.de

^{b)}**Electronic mail:** tokmoldin@uni-potsdam.de

^{c)}**Electronic mail:** shoai@uni-potsdam.de

^{d)}**Author to whom correspondence should be addressed:** neher@uni-potsdam.de

ABSTRACT

The increase in the performance of organic solar cells observed over the past few years has reinvigorated the search for a deeper understanding of the loss and extraction processes in this class of device. A detailed knowledge of the density of free charge carriers under different operating conditions and illumination intensities is a prerequisite to quantify the recombination and extraction dynamics. Differential charging techniques are a promising approach to experimentally obtain the charge carrier density under the aforementioned conditions. In particular, the combination of transient photovoltage and photocurrent as well as impedance and capacitance spectroscopy have been successfully used in past studies to determine the charge carrier density of organic solar cells. In this Tutorial, these experimental techniques will be discussed in detail, highlighting fundamental principles, practical considerations, necessary corrections, advantages, drawbacks, and ultimately their limitations. Relevant references introducing more advanced concepts will be provided as well. Therefore, the present Tutorial might act as an introduction and guideline aimed at new prospective users of these techniques as well as a point of reference for more experienced researchers.

Published under an exclusive license by AIP Publishing. <https://doi.org/10.1063/5.0094955>

I. INTRODUCTION

Considerable improvements have been made over the last few years in the field of organic solar cells, one of the emerging, third-generation photovoltaic technologies. Organic photovoltaics (OPV) distinguish themselves with the potential of a low priced, solution based, scalable production, and their applicability on lightweight, flexible substrates, which are unique selling points of all types of organic electronic technologies.^{1–5} Significant commercial potential can be expected for organic photovoltaics, if certain thresholds in power conversion efficiency (*PCE*), device stability, and production cost are achieved. To be more specific, a study conducted by Darling and You⁶ as well as a more recent cost analysis by

Guo and Min⁷ came to the conclusion that once OPV modules achieve a threshold in performance of $PCE \geq 15\%$, then an impactful and widespread commercial adoption can be expected. This is the case because OPV modules should exhibit significantly shorter energy payback times compared to other types of photovoltaics. In general, most of the organic solar cells employ a two-component active layer in a bulk-heterojunction (BHJ) configuration, thus yielding an interpenetrating network of acceptor and donor materials with an extensive donor:acceptor (D:A) interface (cf. Fig. 1).⁸ The need for these two components and the D:A interface arises from the fact that organic semiconductors exhibit comparatively small dielectric constants of $\epsilon_r \approx 3$.^{9,10} As a result, excitons rather

than free charge carriers, namely, electrons and holes, are formed after photogeneration. The energetic driving force to split the exciton into free charge carriers is obtained at the D:A interface owing to the differences in the energy levels of the donor and acceptor materials. Therefore, the careful matching of the donor and acceptor to drive the generation of free electrons and holes, but also the efficiency to extract electrons and holes from the D:A interface through the BHJ to their respective electrodes is of significant relevance to the ultimate performance of the organic solar cell.

The field of organic photovoltaics has received renewed attention due to the recent performance improvements ($PCE > 18\%$),^{11–13} which can mostly be attributed to the successful use of non-fullerene acceptors (NFAs) that were developed through continuous efforts to replace the hitherto ubiquitous fullerene-based acceptors, such as PCBM.^{14–24} In particular, solar cells based on the polymer donor PM6 and the NFA Y6 are representative for this recent performance increase.^{25–27} Yet, a detailed, in-depth understanding of the relevant loss-processes and the extraction dynamics is necessary for further improvements. In particular, non-geminate recombination, the recombination of electrons and holes that do not originate from the same exciton, has to be curtailed.^{28,29} In general, different non-geminate recombination mechanisms can be categorized by the relationship of the recombination rate $U(t)$ and the charge carrier density $n(t)$,

$$U(t) = \frac{dn(t)}{dt} = -k_{\beta}n(t)^{\beta}, \quad (1)$$

where k_{β} is the recombination coefficient and β is the recombination order. First order recombination ($\beta = 1$; k_1), also commonly known as Shockley–Read–Hall recombination, typically proceeds via trap states deep within the bandgap.³⁰ Second order recombination ($\beta = 2$; k_2), otherwise known as bimolecular recombination, results from direct band-to-band transitions.³¹ Third order recombination ($\beta = 3$; k_3), or Auger recombination, typically only occurs under conditions with very high charge carrier densities that are not relevant for organic solar cells under realistic operating conditions.^{32,33} One noteworthy exception is surface trap-assisted recombination, where the combination of trap states and band bending results in (pseudo) third order processes.^{34–36} In experiments, solar cells tend to exhibit recombination mechanisms with the aforementioned three different orders to a varying degree, depending on the type of device architecture, blend system, temperature, applied voltage, illumination intensity, and many other factors. Nonetheless, the charge carrier density remains the key parameter in the theory of recombination and extraction dynamics, as evidenced by its presence in Eq. (1). Thus, measurement techniques that can be used to quantitatively and accurately determine the charge carrier density of organic solar cells under realistic operating conditions are a valuable tool in the detailed investigation and continued improvement of these devices.

Charge extraction techniques are a common approach to determine the charge carrier density in solar cells.^{37–39} Here, the devices are initially kept under open circuit with constant illumination and are then rapidly switched to the short-circuit (as in charge extraction, CE) or even a reverse bias condition (as in bias-assisted charge extraction, BACE) while at the same time the illumination is switched off. The measured transient current can then be used to

determine the charge carrier density in the device. However, the distinction between charge carriers present in the active layer and other capacitive contributions can be challenging.^{40,41} In the case of charge extraction measurements, the electrode capacitance can be estimated using the device thickness and dielectric constant and is generally not measured directly.³⁷ One approach to make this estimate is to subtract the amount of charge measured when performing the same voltage jump in the dark, starting at 0 V.³⁹ Additionally, charge recombination during the measurement of the current transient may impact the amount of extracted charge. Techniques that instead measure the differential capacitance can circumvent these issues, as they offer an avenue to distinguish between contributions from the active layer, the transport layers, and electrodes. In particular, transient photovoltage and transient photocurrent (TPV/TPC) as well as impedance spectroscopy (IS) and its variation capacitance spectroscopy (CS) are approaches that allow to measure the capacitance resulting from the presence of charge carriers in a solar cell. Ultimately, these techniques offer the opportunity to convert the capacitance to the charge carrier density under realistic operating conditions, if certain assumptions are met and necessary corrections are made, which are presented and discussed in detail during this Tutorial.

II. CAPACITANCE CONTRIBUTIONS FROM DIFFERENT SOURCES

Before we will discuss the aforementioned techniques, it is important to take a detailed look at the different sources that can contribute to the measured capacitance. The geometric capacitance caused by the electrodes and architecture of the device resembling a plate capacitor, and contributions from other layers, such as electron and hole transport layers, are also relevant apart from the chemical capacitance, which is caused by the presence of free charge carriers.

A. Chemical capacitance

The first step in the determination of the density of free charge carriers n is to obtain the chemical capacitance C_{μ} caused by the response of these charge carriers to an electrical or optical perturbation,

$$C_{\mu} = qAL \frac{dn}{dV}, \quad (2)$$

where q is the elementary charge, A is the device area, L is the active layer thickness, and V is the voltage.^{42,43} The relationship described in Eq. (2) is the basis for the subsequent analyses to obtain the charge carrier density n (cf. Sec. IV). However, as we will see throughout Sec. III, the experimental determination of C_{μ} by means of TPV/TPC and IS/CS measurements is not trivial since none of them can directly yield C_{μ} without considering other capacitive contributions to the actual measurement results.

B. Geometric capacitance

The most common contributing factor to the measured capacitance is the geometric capacitance C_g , which depends on the type

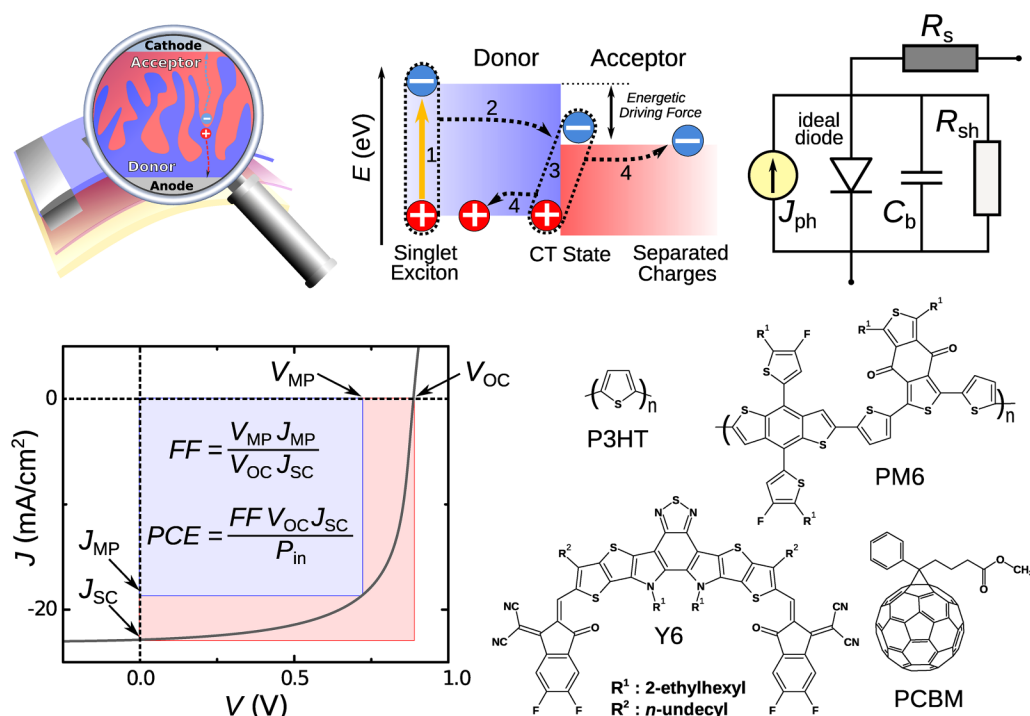


FIG. 1. Schematic depiction of an organic solar cell and its bulk-heterojunction active layer consisting of a donor polymer and acceptor small molecule. The relevant energy levels involved in the photogeneration: (1) formation of exciton via photon absorption; (2) exciton diffusion to the donor:acceptor (D:A) interface and charge transfer (CT) state; (3) charge separation; (4) extraction of free charge carriers to the electrodes. Basic equivalent circuit representing an organic solar cell and its current-density-voltage plot, including the relevant figures of merit. Chemical structures of a fullerene (PCBM) and non-fullerene acceptor (Y6) and two polymer donors (P3HT, PM6).

of electrodes, thickness, and architecture of the device under test. However, for most solar cells, C_g can easily be determined in the dark either at high frequencies, when the carriers within the BHJ are unable to follow the oscillating electric field, or at a relatively high negative bias, when all of the mobile carriers are extracted from the active layer. In this case, the device capacitance is determined entirely by the dielectric properties of the active layer and the device geometry,

$$C_g = \frac{\epsilon_r \epsilon_0 A}{L}, \quad (3)$$

where ϵ_0 is the vacuum permittivity and ϵ_r is the dielectric constant of the active layer. Although the impact of C_g on the total device capacitance should not be neglected, it can have a relatively small contribution in the case of higher carrier generation rates (or illumination intensities), larger forward biases, as well as in devices with high built-in voltages.⁴⁴

C. Contributions from transport layers

The capacitive contributions of the other layers that are commonly employed in organic solar cells, such as electron and hole transporting layers (ETL and HTL), also have to be considered.³² Typically, these transport layers can be modeled by capacitors in

series to the active layer, thus yielding a total capacitance of

$$C_{\text{tot}} = \left(\frac{1}{C_{\text{ETL}}} + \frac{1}{C_{\text{BHJ}}} + \frac{1}{C_{\text{HTL}}} \right)^{-1}. \quad (4)$$

The importance of transport layers can be showcased in an example considering a 40 nm ZnO layer ($\epsilon_{\text{ZnO}} = 4.74$), 80 nm active layer ($\epsilon_{\text{BHJ}} = 3$), and device area of $A = 0.1 \text{ cm}^2$.⁴⁵ In general, the capacitance of each transport layer can be estimated using Eq. (3). In our example, we can expect a capacitive contribution of $C_{\text{BHJ}} = 3.3 \text{ nF}$ from the active layer and $C_{\text{ZnO}} = 10.5 \text{ nF}$ from the ZnO layer. According to Eq. (4), approximately 24% of the total capacitance C_{tot} results from the ZnO layer, an amount that cannot be ignored and must be taken into account in the subsequent analysis. In most cases, a simplification of Eq. (4) is possible, if the transport layers are significantly thinner than the D:A active layer, possess higher relative dielectric constants, and if they are highly doped,

$$C_{\text{tot}} = \left(\frac{1}{C_{\text{ETL}}} + \frac{1}{C_{\text{BHJ}}} + \frac{1}{C_{\text{HTL}}} \right)^{-1} \approx \left(\frac{1}{C_{\text{BHJ}}} \right)^{-1}. \quad (5)$$

Hence, the transport layers observed in isolation would yield higher

values in capacitance, but the reciprocal relationship that describes capacitors in series results in the BHJ active layer capacitor dominating the total measured capacitance. Nonetheless, it is important to consider the influence on the measured capacitance of any layer within the investigated solar cells, whether for TPV/TPC or IS/CS measurements. This is also an aspect that might limit these techniques for other types of devices, such as solar cells based on perovskites, which tend to exhibit significantly larger dielectric constants and typically numerous transport and injection layers, thus making it more challenging to isolate the capacitive contribution of the active layer.⁴⁶

III. EXPERIMENTAL TECHNIQUES

The common goal of differential charging techniques such as TPV/TPC, IS, and CS is to measure the capacitance via a perturbation of the solar cell at different operating conditions, such as different light intensities or applied DC-biases V_{DC} . The solar cell can be perturbed either via a dedicated, fast switching, probing light source (TPV/TPC) or via application of a small AC-voltage V_{AC} (IS/CS). As previously discussed, the main goal is to reliably isolate the chemical capacitance C_{μ} , which is caused solely by the charge carriers in the BHJ active layer. We will discuss this in-depth in Secs. III A–III C by determining the charge carrier density in a high performing PM6:Y6 solar cell.

A. Transient photovoltage and photocurrent

The fundamental working principle of a TPV/TPC measurement to determine the charge carrier density relies on the relationship between the changes of the open-circuit voltage ΔV_{OC} and the charge ΔQ upon application of a small charge carrier density perturbation.⁴⁷ Typically, this perturbation is achieved by applying a short, probing light pulse. Several of these measurements have to be performed at different background illuminations, including in the dark.⁴⁸

1. Setup requirements

The experimental setup to perform a combined TPV/TPC measurement requires two light sources: one spectrally broad, continuously operated light source for the background illumination and one fast-switching, probing light source with intensities well below the background illumination (cf. Fig. 2). Typically, a white LED or a solar simulator can be used for the background illumination, whereas the probing light source should either be a sufficiently fast-switching LED or a laser with a sufficiently small light intensity. The adjustment of the background and probing illumination intensity can be achieved by independently attenuating the electrical power of the white, background LED and the fast-switching probe LED. However, a more convenient approach is the use of neutral density filters for both light sources (background and probe). Thus, once the appropriate ratio between probing and background illumination has been set, which as a rule of thumb should be $I_{probe}/I_{background} < 0.1$, one only needs to change the neutral density filters during the measurements since the ratio of background and probing light intensity should not be affected by the neutral density filters. The solar cell and the two light sources

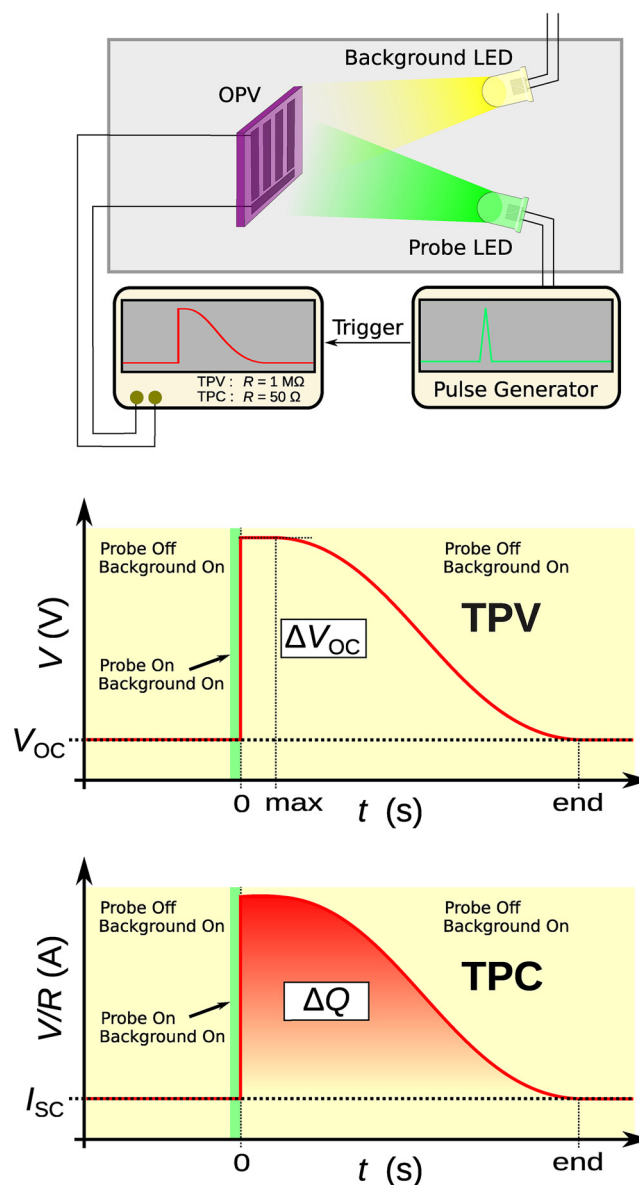


FIG. 2. Experimental setup required to measure the transient photovoltage and transient photocurrent (TPV/TPC) of a solar cell as well as schematic depiction how to determine the perturbation of the open-circuit voltage ΔV_{OC} (for TPV) and of the charge ΔQ (for TPC) caused by the probing light source at varying levels of background illumination.

should be covered or placed inside a container to ensure that no stray light can influence the measurements. A function generator connected to the probing light source can provide the required pulses, while the solar cell should be connected to an oscilloscope, which is triggered by the function generator. The channel of the oscilloscope that is connected to the solar cell should have a high

impedance, typically $1\text{ M}\Omega$, for TPV measurements, and a small impedance, typically $50\ \Omega$, for TPC measurements. Moreover, the RC-time of the external circuit in the TPC measurement should be smaller than that of the solar cell, to ensure that charge extraction occurs rapidly and without any significant losses. In contrast, the RC-time of the external circuit should be larger than that of the solar cell during the TPV measurement, to ensure that the charges recombine within the active layer, rather than by being extracted into the external circuit.

It should be stressed that one TPV and one TPC measurement have to be performed under identical background illumination and probing intensities to obtain any meaningful results.

2. Data acquisition and modeling

The TPV measurement is performed to obtain the change of the open-circuit voltage ΔV_{OC} upon the increase of carrier density by the probe light pulse. Thus, the difference from the background V_{OC} , which forms the relevant baseline, to the maximum of the measured V_{OC} during perturbation, constitutes ΔV_{OC} , as is depicted schematically in Fig. 2 and as can be seen in the experimental results in Fig. 3. The following equation needs to be considered:

$$\Delta V_{\text{OC}} = V_{\text{OC}}(t_{\text{max}}) - V_{\text{OC}}(t_{\text{end}}), \quad (6)$$

where t_{max} is the time at which the measured open-circuit voltage V_{OC} reaches its maximum due to the probing pulse and t_{end} is the end time at which the perturbation caused by the probing pulse has ceased and where the V_{OC} of the background illumination is reached. Hence, it is important to clearly resolve the baseline and the maximum of the V_{OC} . In the case of the TPC measurement, the goal is to obtain the change of the charge ΔQ caused by the probe at the same background illumination as in the TPV experiment. Here, the measurement is performed at the short-circuit condition to monitor the current decay following the switch-off of the probe light.^{49,50} Therefore, in the case of devices in which charge recombination at the short-circuit condition is negligible, the background illumination

is not absolutely necessary for this measurement. However, it should be noted that the oscilloscope can only measure voltages. Thus, the measured voltage needs to be converted first to the current by dividing the voltage by the known impedance of the oscilloscope channel $R = 50\ \Omega$. Then, the measured increase in current caused by the perturbation of the probing pulse must be integrated over time to yield ΔQ (cf. Fig. 2),

$$\Delta Q = \int_{t_0}^{t_{\text{end}}} \left(\frac{V(t)}{R} - J_{\text{SC}} A \right) dt, \quad (7)$$

where t_0 is the initial time at which the perturbation caused by the probing pulse begins, t_{end} is the time at which the perturbation ends, J_{SC} is the short-circuit current density, and A is the area of the organic solar cell. Therefore, the measurement has to be performed in a way that resolves both the baseline and the increased current caused by the perturbation well enough for integration. This can be achieved by averaging several individual measurements during data acquisition, which is a feature offered by most oscilloscopes these days, or by appropriately smoothing the raw data during data analysis. The baseline should be equal to the short-circuit current for the specific background light intensity.

Then, it is possible to calculate the differential capacitance C_{dif} , once ΔV_{OC} and ΔQ have been determined for several background illuminations and, thus, open-circuit voltages V_{OC} . Here it should be noted that,

$$C_{\text{dif}}(V_{\text{OC}}) = \frac{\Delta Q}{\Delta V_{\text{OC}}(V_{\text{OC}})} = C_{\mu}(V_{\text{OC}}) + C_{\text{g}}, \quad (8)$$

where C_{μ} is the chemical capacitance and C_{g} is the geometric capacitance, as described in more detail in Sec. II B.⁵¹ As an example, the experimental values of ΔV_{OC} and ΔQ in Fig. 3 were used to calculate the differential capacitance C_{dif} , as depicted in Fig. 4. This data set also highlights the difficulties of maintaining a small enough probing intensity, specifically at lower background illuminations. On the one hand, a small probing intensity is crucial

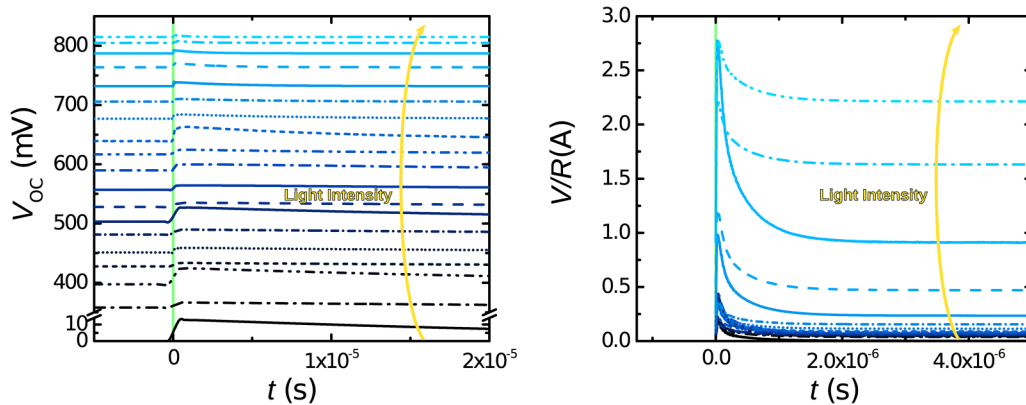


FIG. 3. Absolute transient photovoltage (TPV) $V_{\text{OC}}-t$ plots and absolute transient photocurrent (TPC) $(V/R)-t$ plots at different background illumination intensities of a PM6:Y6 solar cell. The starting point of the perturbation is highlighted in green.

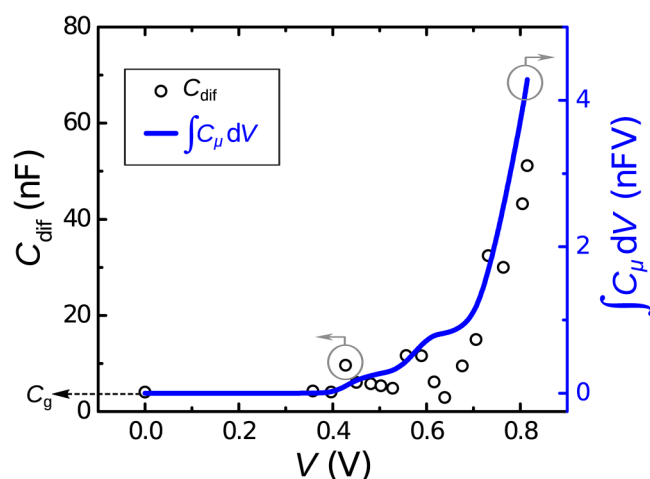


FIG. 4. Differential capacitance C_{diff} of a PM6:Y6 solar cell determined via TPV/TPC at different light intensities (and thus open-circuit voltages), as well as the integral $\int C_{\mu} dV$. The geometric capacitance C_g determined from ΔV_{OC} and ΔQ in the dark is also highlighted.

to avoid any significant influence of the act of probing on the background conditions of the investigated solar cell. But, on the other hand, exceedingly small probing intensities can lead to noisy data. This is especially a problem, if the variations in light intensities are achieved via attenuating the electrical power input of the light sources, as was done in the aforementioned example. However, in most cases, the integration of the capacitance over the relevant voltage range, which is a crucial step in all of the discussed techniques in this Tutorial, to obtain the charge carrier density, will render the impact of noisy C_{diff} values less important (cf. Fig. 4). Integration of the chemical capacitance C_{μ} is the next step to determine the charge carrier density via TPV/TPC measurements. Therefore, it is necessary to exclude any other effects that contribute to the measured, differential capacitance C_{diff} . The most relevant factor that needs to be considered is represented in Eq. (8), where the geometric capacitance C_g is assumed to be the second component together with the chemical capacitance C_{μ} . Experimentally, the geometric capacitance C_g can be determined via the TPV/TPC measurements by turning off the background illumination and performing a measurement without background illumination ($V_{\text{OC}} = 0$). In some cases, particularly for perovskite solar cells, C_g can also be obtained from the plateau that forms at small voltages.

3. Advantages and drawbacks

Overall, TPV/TPC measurements are a straightforward approach to determine the charge carrier density in solar cells. The necessary components to perform these measurements (i.e., function generator, oscilloscope, light sources, and neutral density filters) are readily available in most optoelectronic laboratories and the financial expenses are comparatively limited. Furthermore, only minor corrections of the differential capacitance C_{diff} are necessary to obtain the charge carrier density in the subsequent data analysis.

However, this is also a limitation of the discussed technique, as devices with more complex architectures and with a multitude of other capacity sources cannot be easily analyzed. In addition, the probe light source should exhibit an intensity that results in a voltage increase in the range of $V \approx 10$ mV. Therefore, TPV/TPC measurements are only limited to investigations of solar cells in the forward bias regime and under open-circuit conditions. Thus, the charge carrier density under other important conditions, such as short-circuit maximum-power, or the reverse bias regime is not available.

B. Impedance spectroscopy

The second experimental technique to determine the charge carrier density of a solar cell discussed in detail in this Tutorial is impedance spectroscopy (IS). One of the first steps for any investigation using IS is to build a simplified model of the tested device. Specifically, a reliant equivalent circuit is a powerful tool to model the electrical performance of the device. A very common equivalent circuit model employed for solar cells is depicted in Fig. 1, consisting of an ideal diode, a barrier capacitor C_b , a shunt resistance R_{sh} , and a source of photogenerated charge carriers J_{ph} in parallel as well as a series resistance R_s . It should be noted that the barrier capacitance C_b is equivalent to the differential capacitance C_{diff} used in Sec. III A, but C_b is predominantly used in the literature related to the determination of the charge carrier density via IS. Hence, C_b will also be used in this Tutorial for the relevant capacitance related to IS and CS. The aforementioned, relatively simple model has been successfully employed in previous studies and is sufficient in the context of analyzing J - V -characteristics.^{43,52,53} However, more complex equivalent circuits will be necessary for some analyses based on IS as we will see later in-depth.

1. Setup requirements

Experimentally, IS measurements are performed by applying small-amplitude perturbations in form of an AC-voltage V_{AC} at various applied biases V_{DC} and background illuminations. Similar to the TPV/TPC approach, the AC-voltage V_{AC} must be small in comparison to the applied DC-voltage V_{DC} , otherwise the perturbation required for the IS measurement would start to overshadow the chosen background conditions. At the same time, an AC-voltage V_{AC} that is too small leads to noisy data. Typical values chosen for the AC-voltage are in the range of $V_{\text{AC}} = 5$ – 40 mV, as reported in the literature.^{26,47,54} In contrast to TPV/TPC, the experimental setup only needs one constant light source since the perturbations are achieved electrically (cf. Fig. 5). IS may be performed using various types of testing equipment: LCR-meters, impedance analyzers, or vector network analyzers. Although the measurement theory and operation in all of these instruments differ, they usually provide equivalent results within the measurement uncertainty range.⁵⁵ However, there are options for more specialized equipment that focus specifically on a certain frequency range, relevant for electrochemical reactions, batteries, solar cells, or high frequency electronics.^{56–63} Most dedicated IS equipment nowadays include software to perform the fitting of the experimental data by adjusting the equivalent circuit model, which facilitates and accelerates the data analysis. In terms of investigating organic solar cells, it is

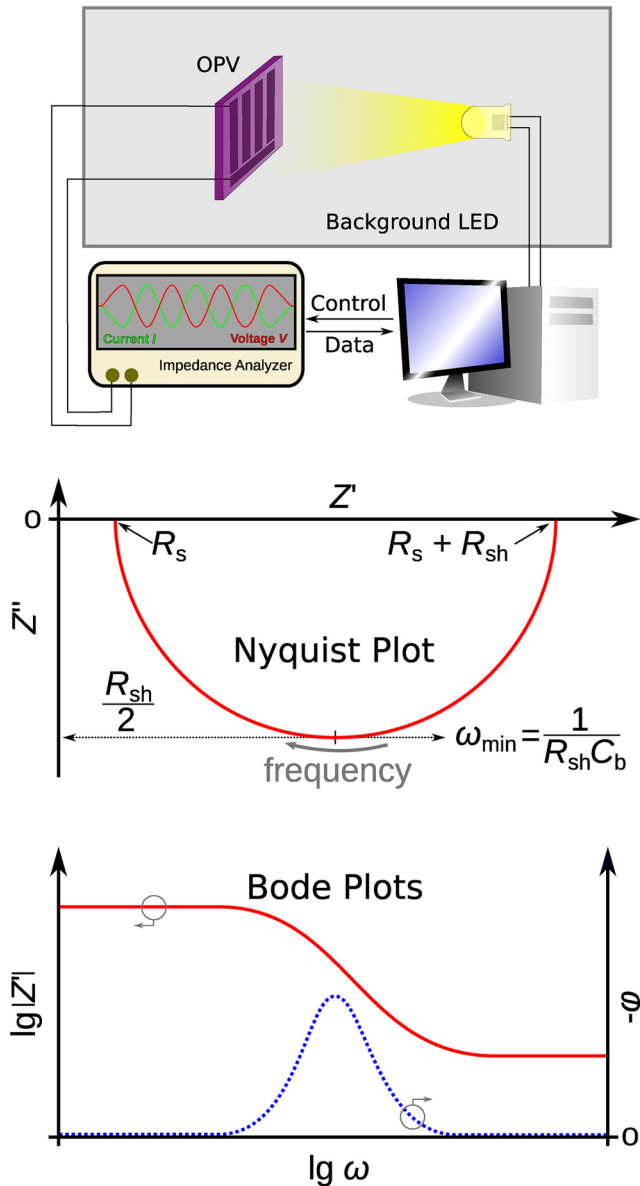


FIG. 5. Experimental setup required for impedance spectroscopy measurements of a solar cell as well as schematic depiction of a Nyquist plot and the two Bode plots.

possible to employ already existing setups used for other techniques, such as J - V -characteristics, which include a light source, such as white LEDs or a solar simulator and other accessories, such as neutral density filters or temperature control stages.^{64,65} It is advisable to use short, shielded cables and a Faraday cage, specifically to improve the measurement results at higher frequencies. One very important peculiarity of IS that is often overlooked is the necessity to illuminate the entirety of the device, when conducting

IS measurements under illumination. J - V -measurements of solar cells are often performed with a mask in front of the device under test. This is done to perform the measurement with a standardized illuminated area that is determined by the mask, not the solar cell. Thus, the current density J is readily available during measurements since the area of the mask is not dependent on the small variations of the active area between individual devices. This practice has been implemented to exclude any edge effects that might particularly influence the accuracy of the measured short-circuit current density J_{SC} , although the use of masks might also negatively influence the accuracy of the measured V_{OC} and FF . In general, the measurements with masks do not significantly influence the J - V -characteristics as long as correctly sized masks are employed and a proper alignment is achieved.⁶⁶ However, this is not the case during the investigation of solar cells via IS measurements with such an aforementioned mask. Effectively, one measures an illuminated and a dark solar cell in parallel, if IS measurements with a mask and, thus, a partly illuminated solar cell are performed. Indeed, such a case could be modeled appropriately with more complex equivalent circuits that include the distinction between dark and illuminated parts, as depicted in Fig. 6. However, it would still be necessary to measure the exact area of the device to determine the dark area. Therefore, it is more reasonable to simplify the needed equivalent circuit by measuring only fully illuminated devices. If necessary, an accurate determination of the area of a solar cell can be achieved by photographing the device and a scale reference with a high contrast ratio, opening the photo in a common image manipulation software, selecting the area in question with the color similarity selection tool, and converting the selected pixels to a useful unit of area.

2. Fundamental principles

In general, a sinusoidal voltage signal is applied to the device under test during an impedance measurement,

$$V(t) = V_0 \cos(\omega t), \quad (9)$$

causing a response current,

$$I(t) = I_0 \cos(\omega t - \varphi), \quad (10)$$

where V_0 and I_0 are the voltage and current amplitudes, ω is the angular frequency, and φ is the phase shift between the voltage and current signals. Now, using Euler's sinusoidal-to-exponential transformation, the frequency-dependent ratio of the voltage and current is defined as a complex resistance, otherwise also known as impedance,

$$Z = \frac{V_0}{I_0} e^{i\varphi} = Z_0 \cos \varphi + i Z_0 \sin \varphi = Z' + i Z'', \quad (11)$$

where Z_0 is the impedance amplitude and Z' and Z'' are the resistance (active part) and reactance (imaginary part) of the circuit, respectively. The combination of all resistance components can be represented through the active part Z' . In turn, the imaginary part Z'' accounts for the capacitive and inductive contributions, such as barrier capacitance C_b and parasitic inductance L_{ind} (cf. Sec. III C).

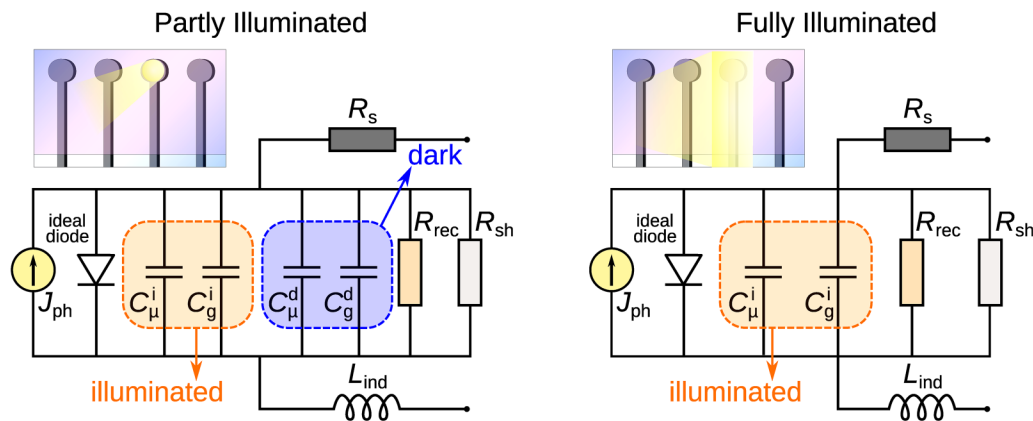


FIG. 6. Schematic representation of a partly and fully illuminated solar cell as well as their respective equivalent circuit models.

Each of these contributions dominates the total impedance of the device at different frequencies, with its value at various frequency ranges and applied voltages enabling to determine individual contributions.

3. Nyquist plots

In practice, the first step of an IS analysis relies on a Nyquist plot, depicting the relationship between the real and imaginary parts of the impedance. This is conceptually shown in Fig. 5 for an organic solar cell with the simple equivalent circuit described previously. The Nyquist plot of such an ideal parallel connected R - C -circuit resembles a semi-circle, where each point corresponds to a certain frequency. At low frequencies and thus high Z' values, one can determine the sum of the series resistance R_s and shunt resistance R_{sh} . Alternatively, in the middle frequency range, one can also determine half of the shunt resistance R_{sh} either via the distance from the onset to the minimum of the semi-circle over the Z' -axis or via the absolute value of the reactance Z'' at the minimum of the semi-circle. In addition, the capacitive elements such as the barrier capacitance C_b are accessible at the angular frequency ω_{min} , at which Z'' reaches its most negative value,

$$\omega_{min} = \frac{1}{R_{sh} \times C_b}. \quad (12)$$

Thus, it is possible to obtain values for the capacitance relevant for the calculation of the charge carrier density via well resolved Nyquist plots, if the relatively simple equivalent circuit model described in Fig. 1 is sufficient for the description of the investigated organic solar cell. Furthermore, the distance from the origin of the reference system to the onset of the semi-circle indicates the value of the series resistance R_s , which occurs at a high frequency and, thus, low Z' values.

4. Bode plots

Another commonly used form to display IS measurements is via Bode plots, which are a way to specifically show the frequency response of a tested device. Typically, two types of Bode plots are necessary, the first showing the magnitude $|Z'|$ and the second the phase φ in relationship with the angular frequency ω . A combined Bode plot consisting of the $\lg|Z'|$ - $\lg\omega$ - and φ - $\lg\omega$ -plots for a solar cell with the aforementioned simple equivalent circuit is depicted in Fig. 5. One particular advantage of Bode plots in comparison to a Nyquist plot is that the frequency-dependent behavior is clearly resolved. The value of the phase indicates resistive ($\varphi = 0$), inductive ($\varphi = +90$, not present in the circuit model shown in Fig. 5), and capacitive ($\varphi = -90$) behavior.

5. Advanced circuit models

However, the simple equivalent circuit that has been used up to now is often not sufficient to realistically model organic solar cells. Hence, more elaborate equivalent circuits need to be explored, such as the one depicted in Fig. 7. In this elaborate model, there are three additions to the simpler model described previously. First, the barrier capacitance C_b has been replaced by the chemical capacitance C_μ and the geometric capacitance C_g in a similar fashion as described in Sec. III A, specifically Eq. (8). Second, a recombination resistance R_{rec} parallel to the shunt resistance R_{sh} has been added,

$$R_{rec} = \left(\frac{1}{R_{bm}} + \frac{1}{R_{mm}} + \frac{1}{R_{sf}} \right)^{-1}, \quad (13)$$

where R_{bm} is the recombination rate of bimolecular recombination, otherwise known as band-to-band recombination, R_{mm} is the recombination rate of monomolecular recombination, otherwise known as bulk trap-assisted recombination or Shockley–Read–Hall recombination, and where R_{sf} is the recombination rate of surface trap-assisted recombination.³⁵ In this example, it is assumed that these three types of recombination processes do not influence each other and can be described in a superposition manner. The third

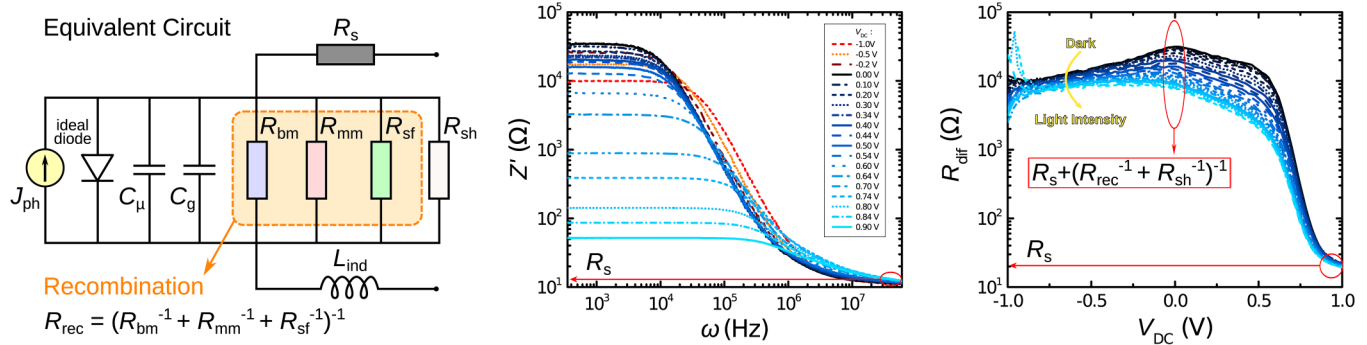


FIG. 7. Equivalent circuit comprised of the series resistance R_s , shunt resistance R_{sh} , recombination resistance R_{rec} , ideal diode, geometric capacitance C_g , chemical capacitance C_μ , and parasitic inductance L_{ind} . The recombination resistance R_{rec} can be interpreted as superposition of different types of mechanisms, such as bimolecular (bm), trap-assisted or monomolecular (mm), as well as surface trap-assisted (sf) recombination.³⁵ The estimation of some of the aforementioned components via a Z'' - ω -plot resulting from impedance spectroscopy measurements with different applied biases V_{DC} in the dark and a R_{diff} - V_{DC} -plot resulting from J - V -curves at different light intensities is also shown for a PM6:Y6 solar cell.

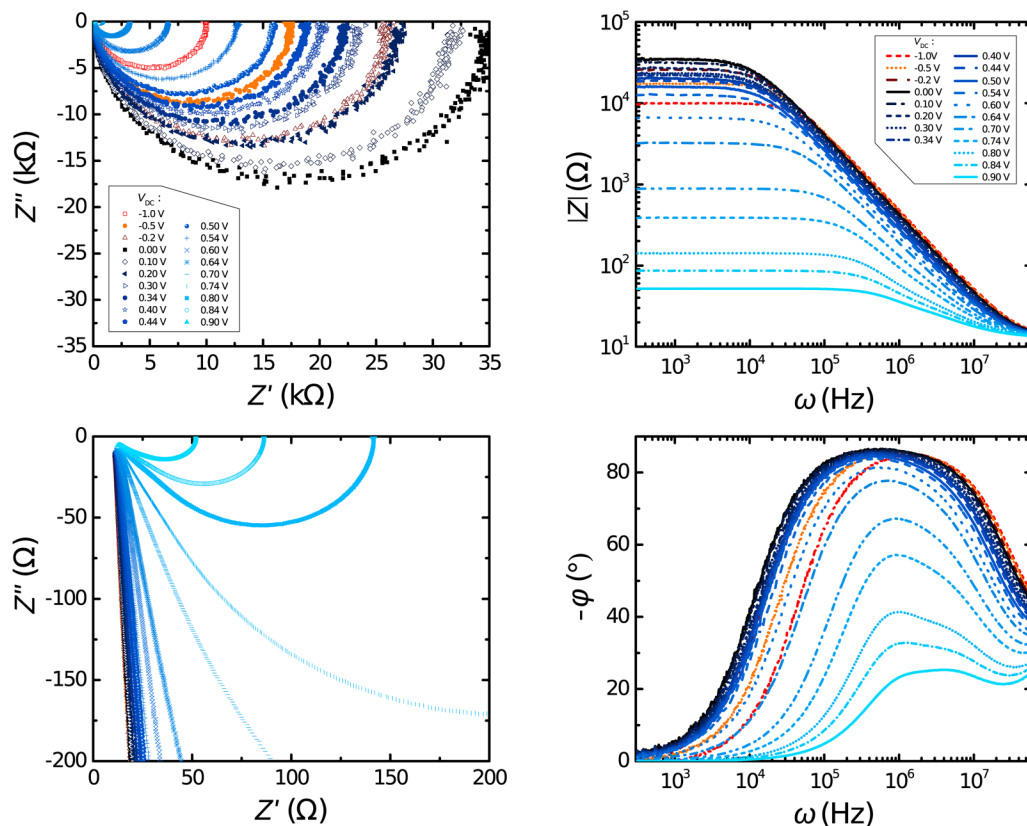


FIG. 8. Nyquist plots at different scales and Bode plots (absolute impedance $|Z|$ - ω - and ϕ - ω -plots) of a PM6:Y6 solar cell with different applied biases V_{DC} in the dark.

addition is an inductance L_{ind} related to the parasitic inductance caused by the connections to the device. As we will see later, the inclusion of L_{ind} is most relevant at higher frequencies. However, certain proprietary IS setups can account for these parasitic effects via initial compensation measurements.

There are other examples of equivalent circuits, where the contributions of transport layers and certain types of recombination processes are assumed to be in series with the chemical capacitance C_{μ} , rather than in parallel.^{47,67} Transmission line equivalent circuit models to describe the conduction of charges with ohmic contacts, lumped circuit models, and models incorporating constant-phase-elements (CPEs) are also frequently used in IS.^{57,68–70}

6. Experimental results

The experimental results of an IS measurement of a PM6:Y6 solar cell are shown in Figs. 7 and 8. The $Z'-\omega$ -plot at different applied biases V_{DC} in the dark depicts how the series resistance R_s can be determined from the converging Z' values at a high angular frequency ω . For comparison, the series resistance R_s can also be determined via the differential resistance R_{dif} available from the J - V -characteristics,

$$R_{\text{dif}} = \frac{dV}{dI}, \quad (14)$$

where I is the current. At sufficiently high forward bias, $R_{\text{dif}} \rightarrow R_s$, whereas at a bias of $V_{\text{DC}} = 0$ one can estimate R_{sh} and R_{rec} .^{54,71} Indeed, as shown in the $R_{\text{dif}}-V_{\text{DC}}$ -plot at different illumination intensities in Fig. 7, the values for the series resistance are in a comparable range, irrespective if they were determined via IS measurements or J - V -characteristics. In addition, the Nyquist and Bode plots of the experimental data also exhibit deviations from the previously discussed, simple model. It can be seen that the lower frequency regions of these plots are rather noisy and do not clearly resolve the intersection of the measured Z'' values with the Z' -axis. However, it is still possible to determine the shunt resistance R_{sh} and through extrapolation, the value for the barrier capacitance C_b —as described in Eq. (12). Averaging more measurements and reducing the starting angular frequency ω should better resolve the low frequency regions. However, one has to consider that these changes would incur a significant increase in the measurement time, depending on the chosen initial frequency and the amount of averaged data sets. Hence, a balance between measurement time and resolution at lower frequencies has to be found since extended measurement times can also cause degradation of the tested device. The Nyquist plot in the high frequency range is quite similar to the idealized picture in Fig. 5, although there are still some deviations, such as $Z'' > 0$, which is likely linked to parasitic effects. The two Bode plots of the experimental data shown in Fig. 8 deviate also from the idealized model. Specifically, the φ - ω -plot exhibits a baseline effect that shifts the data sets upward at higher angular frequencies, which can be related to the presence of additional capacitive contributions, such as the Maxwell displacement current capacitance (cf. Sec. III C 3). In contrast, the $|Z|$ - ω -plots coincide quite well with what would be expected from the idealized model. The goal of IS measurements is to obtain

values for the chemical capacitance C_{μ} , similar to the TPV/TPC measurements as discussed in Sec. III A. Hence, it is necessary to choose an appropriate equivalent circuit model, which includes C_{μ} , and to analyze the experimental data, which is typically presented via a Nyquist plot or Bode plots (cf. Fig. 8). Concomitantly, the values of the other components of the chosen equivalent circuit will also be available, which offers further insight into the processes and properties of the investigated organic solar cell. However, the analysis should first be tried with a quite simple equivalent circuit model, similar to what has been depicted in Fig. 1, to avoid the risk of over-fitting. Each component within the equivalent circuit that ensures a reasonable analysis of the experimental data must relate to some physical analog, such as the resistance of a transport layer, or the capacitance of an interlayer of the tested device, to just name two examples. Otherwise, the results might not provide any meaningful data. Furthermore, at least part of the results should be referenced with independent measurements. In the case of organic solar cells, J - V -characteristics can yield estimates for the series resistance R_s and shunt resistance R_{sh} (cf. Fig. 7). The geometric capacitance C_g can be estimated based on Eq. (3). Typically, the blends of donor and acceptor materials tend to exhibit a relative dielectric constant of $\epsilon_r \approx 3$.^{9,10} The experimental data shown in Fig. 8 were used to determine the barrier capacitance C_b via Eq. (12) for the tested PM6:Y6 solar cell in the dark and under illumination, which is shown in Fig. 9.

7. Advantages and drawbacks

The advantages of the IS approach are apparent when comparing the results of IS and TPV/TPC depicted in Figs. 4 and 9, respectively. First, IS offers the opportunity to measure under

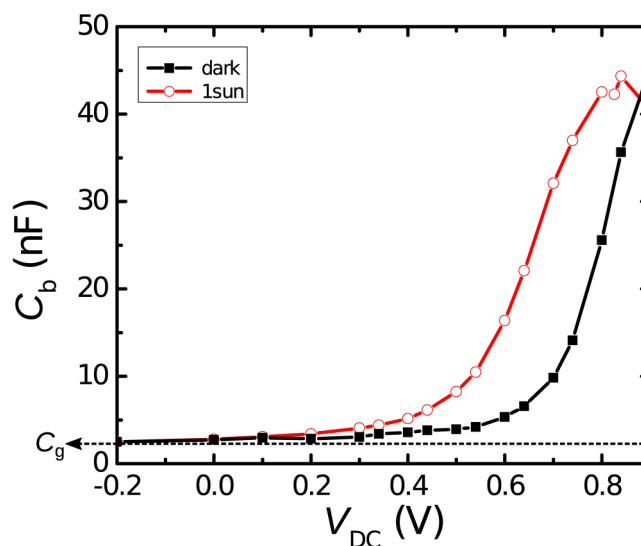


FIG. 9. Barrier capacitance C_b in dependence of the applied bias V_{DC} of a PM6:Y6 solar cell determined via IS in the dark and under simulated 1 sun illumination. The determined geometric capacitance C_g is also highlighted.

conditions other than open-circuit. Second, the data compared in this example are less noisy for the IS approach. As we will see later, the influence of the noise on the overall determination of the charge carrier density is less pronounced. Overall, IS measurements and the subsequent analyses offer a broad set of insight with regard to the investigated devices. In the case of organic solar cells, the charge carrier density can be determined at different applied biases V_{DC} and illumination intensities. Thus, more operating conditions are available than with the TPV/TPC approach, including short-circuit, maximum-power, and even the reverse bias regime, although meaningful measurements in this range are more challenging. If the IS measurements are coupled with J - V -characteristics at identical conditions, one can obtain in-depth information on charge carrier mobility, recombination, and extraction dynamics, as well as charge carrier drift and diffusion lengths.^{54,64,72–74} Some studies have also related IS results to the energetic disorder of the density of states and energetic distribution of trap states in organic solar cells.^{75–78} However, as discussed previously, performing meaningful IS measurements and analyses requires more dedicated hardware and careful considerations than the TPV/TPC method.

C. Capacitance spectroscopy

Another approach to obtain the charge carrier density is via a variation of IS, namely, capacitance spectroscopy (CS). The experimental setup and measurement considerations are identical to IS (cf. Sec. III B 1). However, rather than fitting the Nyquist plot, one assumes a reasonable equivalent circuit, such as the one illustrated in Fig. 7, and calculates the barrier capacitance C_b , including necessary corrections, at different applied biases V_{DC} , and illumination intensities, over a large part of the frequency range. Typically, one would at first use the IS approach discussed in Sec. III B, as it offers a way to investigate the right equivalent circuit model through the analysis of the Nyquist plot.

1. Fundamental principles

The barrier capacitance C_b of a solar cell is a function of frequency, applied voltage, as well as illumination intensity and can be generally represented as a sum of two terms: the charge carrier density independent term of the geometric capacitance C_g , and a frequency, applied voltage, and light intensity dependent term, which is assumed to be the chemical capacitance C_μ . Thus, an analogous expression to Eq. (8) that is used in the TPV/TPC approach can be formulated as

$$C_b(\omega, V_{DC}) = C_\mu(\omega, V_{DC}) + C_g. \quad (15)$$

However, it should be noted that Eq. (15) is only valid, if the material of the BHJ active layer can be considered as an intrinsic semiconductor. In contrast, a doped system will contain additional voltage-dependent capacitance contributions to the chemical capacitance C_μ , namely, the voltage-dependent Maxwell displacement current capacitance of the depletion region C_M , as described in more detail in the literature.⁵⁴ The value of the geometric capacitance C_g can be obtained via the methods discussed in Sec. II B and verified via Eq. (3) since the dielectric constant should not significantly deviate from the expected value of $\epsilon_r \approx 3$.^{9,10}

2. Additional corrections

For a standard organic solar cell, the capacitive contribution is dominant over the inductive contribution across a wide measurement range, up to high angular frequencies of $\omega \approx 1$ MHz. This is also clearly visible in the φ - ω -plot depicted in Fig. 8, where a phase shift of $\varphi \approx -90^\circ$ indicates dominant capacitive contributions. In such a

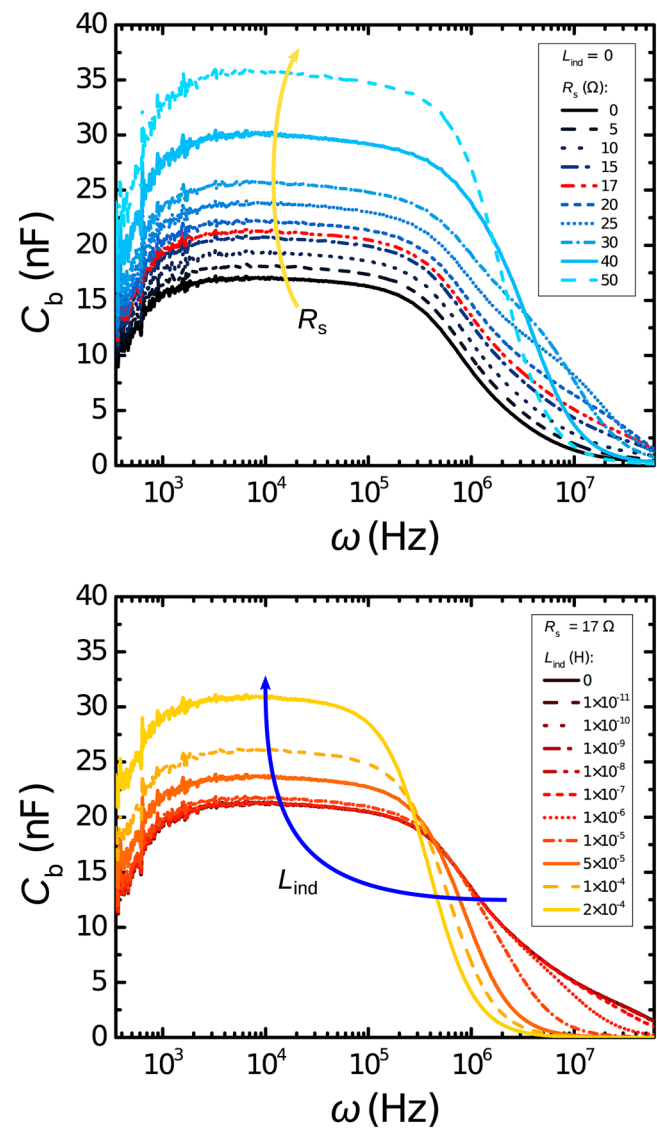


FIG. 10. Barrier capacitance C_b of a PM6:Y6 solar cell in the dark (Fig. 8) calculated via Eq. (16) from the frequency dependence of the impedance and at a constant applied bias of $V_{DC} = 0.8$ V for different values of the series resistance R_s (top) and parasitic inductance L_{ind} (bottom). The Z' - ω -plot in Fig. 7 reveals a series resistance of $R_s = 17 \Omega$ (top, red dashed dots), while the initial compensation measurement of the vector analyzer accounted for the parasitic inductance ($L_{ind} = 0$).

case, taking into account the effects of series resistance and parasitic inductance in the circuit, the barrier capacitance is given by⁶⁷

$$C_b = -\frac{1}{\omega} \left[\frac{Z'' - \omega L_{\text{ind}}}{(Z' - R_s)^2 + (Z'' - \omega L_{\text{ind}})^2} \right]. \quad (16)$$

As is highlighted in Fig. 10, the precise determination of the series resistance R_s and parasitic inductance L_{ind} is quite important in extracting the correct C_b spectrum. In this example, a PM6:Y6 solar cell was measured in the dark at an applied bias of $V_{\text{DC}} = 0.8$ V. It is obvious that the series resistance R_s has a significant influence on the calculated barrier capacitance C_b , specifically in the mid angular frequency range of $\omega = 10^3 - 10^6$ Hz, which is of crucial importance for the subsequent analyses. The parasitic inductance, in contrast, only exhibits a notable effect on that specific angular frequency range, if for this example unreasonably high values are selected ($L_{\text{ind}} > 10^{-5}$ H). However, the parasitic inductance has a stronger influence on the barrier capacitance C_b at high angular frequencies ($\omega > 10^6$ Hz). It should be noted that in this example the initial compensation measurement of the used vector analyzer accounted for the parasitic inductance of the connecting cables.

3. Experimental results

The dependence of the barrier capacitance C_b on the applied bias V_{DC} , the angular frequency ω , and the light intensity is depicted in contour plots for a comparatively high performing PM6:Y6 solar cell in the dark and under 1 sun illumination (cf. Fig. 11). This experimental example shows the importance of selecting the correct frequency range to determine the capacitance C_b . In the shown example, a frequency range close to $\omega = 10^5$ Hz is the best choice since lower frequencies will be subject to noisy data and to negative capacitance values, which are likely related to the presence of traps.^{79–82} At larger frequencies, C_b decreases since not all charge carriers in the device are able to follow the applied AC-signal. Hence, as a rule of thumb, one should search for the frequency range where the barrier capacitance C_b exhibits a plateau throughout all applied biases V_{DC} and illumination intensities. The C_b - ω -plots in Fig. 11 reveal that this rule of thumb is adhered to at an angular frequency of $\omega = 10^5$ Hz. Furthermore, the C_b - V_{DC} -plots in Fig. 11 show the deviations incurred by the different choices of the angular frequency ω . In comparison to the chosen angular frequency of $\omega = 10^5$ Hz, lower and higher angular frequencies tend to underestimate C_b ,

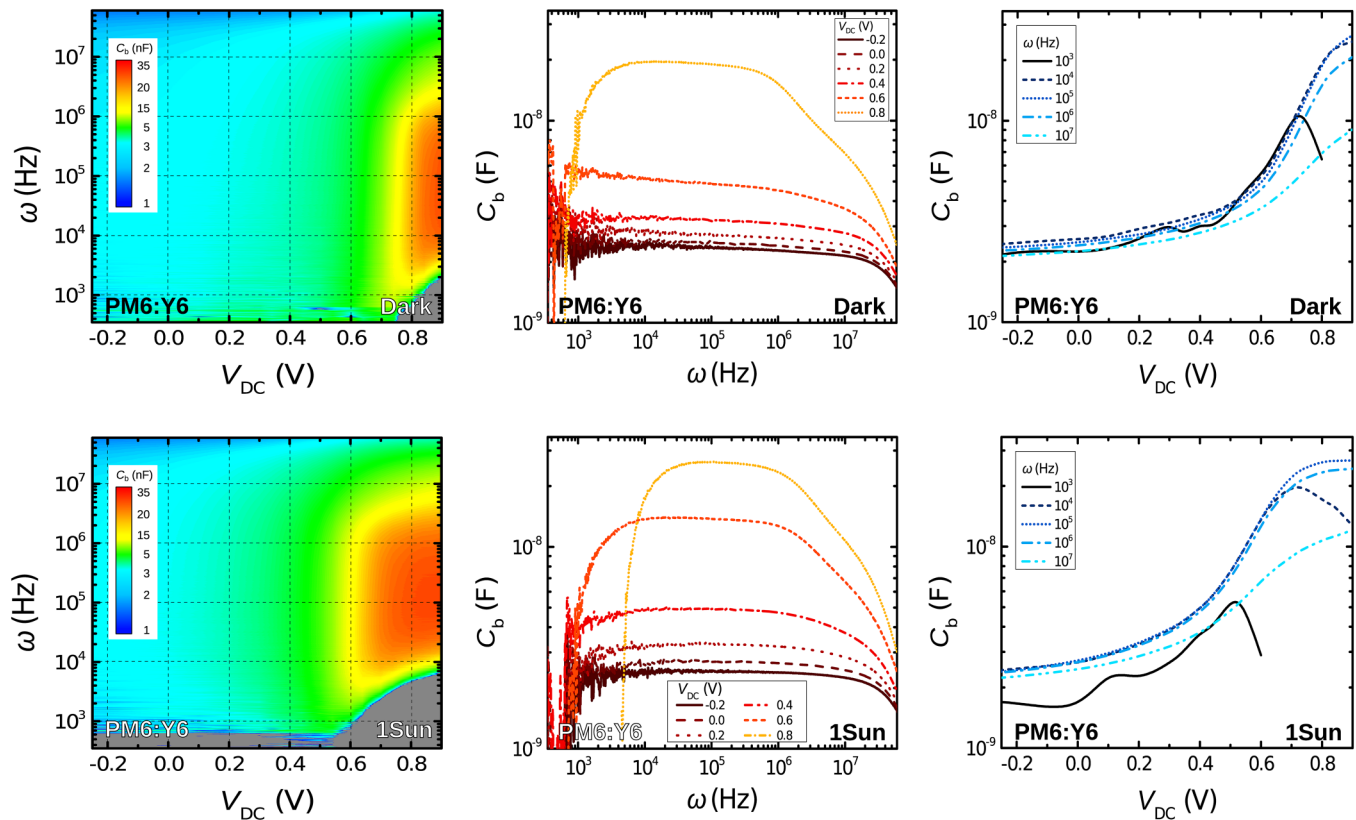


FIG. 11. Barrier capacitance C_b in dependence of the applied voltage V_{DC} and the angular frequency ω for a PM6:Y6 solar cell in the dark and under 1 sun illumination. Areas with undefined values (e.g., $C_b < 0$) are denoted in gray.

specifically at forward biases. This observation is the case for measurements in the dark as well as under 1 sun illumination. These differences have a significant influence on the ultimately calculated charge carrier density, since according to Eq. (15) the barrier capacitance C_b is directly linked to the chemical capacitance C_μ . Thus, choosing the angular frequency incorrectly would lead to underestimated charge carrier densities, specifically at forward biases. Finally, the selection of the frequency range for determination of C_b is important in terms of the RC-limitation, as the respective RC-time inversely relates to the cutoff frequency of the impedance measurement for the studied system.

It is possible to directly measure C_b - V_{DC} -plots at a specifically chosen angular frequency ω and most experimental setups offer this option. Such an approach can yield faster measurements in comparison to the exploration of a broad frequency range. However, a correct frequency has to be chosen (typically one where C_b is constant), otherwise this would result in an incorrect chemical capacitance C_μ . More sophisticated interpretations of the relationship between the chemical capacitance C_μ and the barrier capacitance C_b include the aforementioned voltage-dependent capacitance C_M , which becomes important in situations, where the depletion width is smaller than the active layer or in case of doping. Further details about these more complex models, which can be used to fit the C_b - ω -plots, and the decreasing capacitance at higher frequencies, can be found in the literature.^{54,83} In general, great care has to be taken in the selection of the relevant angular frequency and a V_{DC} - ω - C_b -plot is a good, exploratory tool in this endeavor.

Low performing solar cells tend to exhibit the aforementioned plateau of C_b values at lower angular frequencies.^{24,57,83} This is likely linked to reduced carrier mobilities and/or low carrier lifetimes, which can cause a so-called carrier freeze-out, particularly for thick devices.⁸⁴ Moreover, it can happen that there is a wide range of applied biases V_{DC} at which comparatively high C_b values can be observed, mostly in the measurement of the illuminated device, but also in the dark. This exemplifies a problem related to the determination of the geometric capacitance C_g and chemical capacitance C_μ that can cause problems in low performing organic solar cells. First, even at a small reverse bias in the dark, the C_b - ω -plot can imply the presence of charge carriers in the device, thus not being a reasonable estimate for C_g . Second, at a small reverse bias under illumination, similar C_b values can be measured in comparison to the forward bias regime. Hence, it also implies the presence of a substantial amount of photogenerated charge carriers at small reverse bias under illumination (cf. Sec. IV B). Either the charges are not extracted and remain in the device, even at reverse bias, or there is another source for the comparatively large barrier capacitance C_b , such as trap states. One potential remedy for this problem is to measure the barrier capacitance C_b at substantially larger reverse biases (e.g., $V_{DC} \approx -3$ V) in hopes of reaching a point where the supposedly not extracted charge carriers are finally extracted. However, increased reverse bias values entail the risk of degrading the tested solar cells. Analyzing the measured C_b -data may still lead to an inaccurate estimate of the chemical capacitance C_μ , by interpreting the large C_b values purely as resulting from charge carriers, which leads to overestimated charge carrier densities. Hence, CS can come to its measurement limits for

low performing devices, something that has also been observed in the TPV/TPC approach.⁸⁵

4. Advantages and drawbacks

In summary, the CS approach complements analyses based on IS that were discussed in Sec. III B and offers more in-depth insight, specifically in relation to the capacitance properties of the tested solar cells. CS relies heavily on the correct choice of the equivalent circuit, thus requiring IS measurements beforehand. However, once the validity of an equivalent circuit model for a type of device has been established, the CS approach can yield quicker results with similar accuracy.⁴³

IV. DETERMINATION OF THE CHARGE CARRIER DENSITY

Once the chemical capacitance C_μ has been determined, regardless whether via TPV/TPC or IS/CS measurements, it is possible to calculate the charge carrier density according to Eq. (2). However, previous studies related to IS/CS have brought up the question, whether the total charge carrier density n_{tot} has to include contributions from voltage independent sources as well. In general, a voltage independent, saturated charge carrier density n_{sat} and a voltage-dependent, excess charge carrier density $n_{\text{exc}}(V)$ were postulated in these studies.^{43,54,64,83} The total charge carrier density n_{tot} would then be defined as

$$n_{\text{tot}}(V) = n_{\text{sat}} + n_{\text{exc}}(V). \quad (17)$$

A. Excess charge carrier density

The excess charge carrier density n_{exc} can be obtained from the fundamental relationship between the charge carrier density and the chemical capacitance as described in Eq. (2),

$$n_{\text{exc}}(V) = \frac{1}{qAL} \int C_\mu dV. \quad (18)$$

It is still up for debate whether Eq. (18) alone describes the excess charge carrier density with sufficient accuracy for devices under illumination when analyzing IS/CS measurements. Some studies suggest to take the excess charge carriers for the device in the dark into account by subtracting it from the values for the device under illumination (i.e., $n = n_{\text{light}} - n_{\text{dark}}$), while in other studies this aspect is not explicitly considered.^{83,86} Moreover, the boundary conditions for the integration depicted in Eq. (18) have to be specified. In the case of TPV/TPC measurements, the lower boundary will be a voltage of $V = 0$, which coincides with the measurement in the dark, which is necessary to determine the geometric capacitance C_g . The upper bound will be equal to the highest open-circuit voltage V_{OC} that should have been obtained under the conditions with the highest background illumination, resulting in the following relationship:

$$n_{\text{exc}}(V_{OC}) = \frac{1}{qAL} \int_0^{V_{OC}} C_\mu dV_{OC}. \quad (19)$$

The integration shown in Eq. (19) is, in general, performed over open-circuit voltages V_{OC} since this is the only condition at which TPV/TPC measurements can be performed.

In the case of IS/CS measurements, the selection of the boundaries is more complex. The upper boundary typically is the open-circuit voltage V_{OC} , but it conceivably can be even higher, if measurements with applied biases beyond the open-circuit voltage ($V_{DC} > V_{OC}$) were performed. This case usually occurs at lower illumination intensities. As a rule of thumb, the lowest applied bias V_{DC} measured should be chosen as the lower boundary. Hence, the lower boundary condition can extend into the reverse bias since it is possible to measure IS/CS at $V_{DC} < 0$. This bias is also commonly referred to as the saturation voltage V_{sat} at which the capacitance should converge to the geometric capacitance C_g when measured in the dark.⁴³ Another unique property of the IS/CS approach in comparison to the TPV/TPC approach is that not only measurements at open-circuit conditions can be performed. Hence, the influence of the series resistance R_s on the voltage has to be taken into account. The correction of the applied bias is usually important in the scope of J - V -characteristic, but the same approach can be used for IS/CS measurements as well. In general, it is assumed that a part of the applied bias V_{DC} is lost over the series resistance R_s . This effect can be corrected as follows:

$$V_{cor} = V_{DC} - J \times R_s, \quad (20)$$

where J is the current density and V_{cor} is the corrected voltage. Therefore, the integration of the chemical capacitance C_μ that is necessary to calculate the excess charge carrier density has to be performed after the applied bias V_{DC} has been converted to the corrected voltage V_{cor} . Thus, the following variation of Eq. (18) is appropriate for IS/CS:

$$n_{exc}(V_{cor}) = \frac{1}{qAL} \int_{V_{sat}}^{V_{OC}} C_\mu dV_{cor}. \quad (21)$$

Whether V_{DC} or V_{cor} is used during the integration can yield different results, as shown in Fig. 12. In this example, the excess charge carrier density of a high performing PM6:Y6 solar cell is determined either by integrating over V_{DC} or V_{cor} . There is no significant difference in the determined excess charge carrier densities n_{exc} between the two approaches at lower voltages. However, the $n(V_{cor})$ values are up to 14% smaller than their respective $n(V_{DC})$ counterparts at voltages between maximum-power and open-circuit conditions. This is caused by the pronounced change in current density in this voltage region. It should be noted that these deviations are exacerbated with increasing values of the series resistance R_s , which typically render the aforementioned corrections more important for low performing devices. Such corrections are not necessary, if the TPV/TPC approach was used to determine the chemical capacitance C_μ since the series resistance R_s does not have any influence on the value of the open-circuit voltage V_{OC} . This fact can be easily understood, if one considers Eq. (20) under open-circuit conditions, where the current-density should approach $J = 0$.

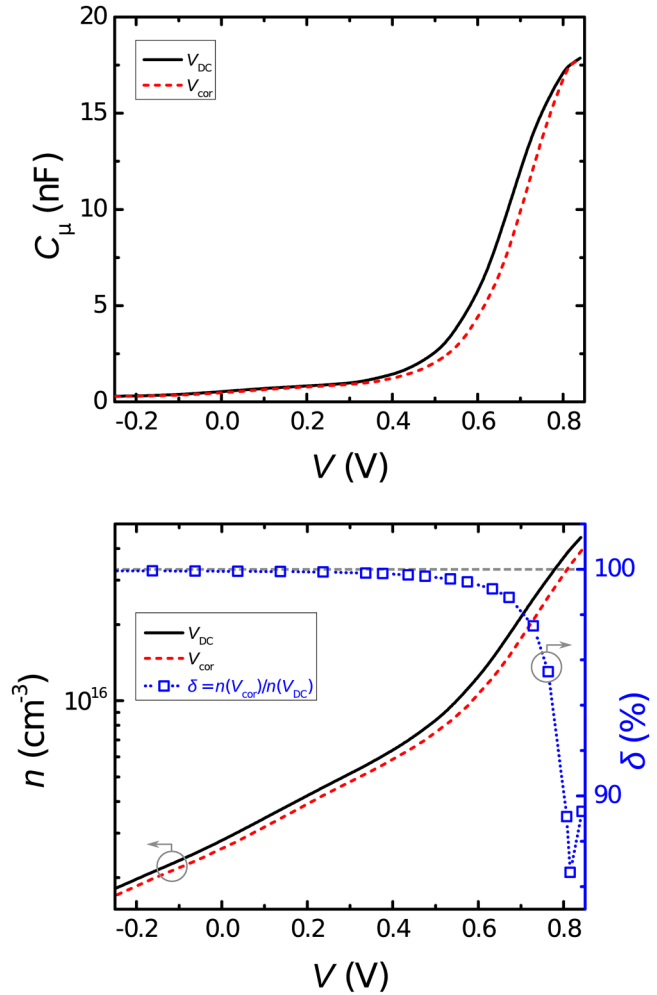


FIG. 12. Comparison of the chemical capacitance C_μ plotted against the applied bias V_{DC} or the corrected voltage V_{cor} for a PM6:Y6 solar cell under 1 sun illumination. The influence of the different C_μ - V -plots on the excess charge carrier density n_{exc} is shown as well, including the relative changes δ .

B. Saturated charge carrier density

The second contributing factor to the total charge carrier density is the voltage independent saturated charge carrier density n_{sat} , which can be calculated in the simplest way via the difference in capacitance at reasonably high reverse bias ($V_{sat} \leq -1V$) in the dark and under illumination,

$$n_{sat} = \frac{1}{qAL} \times [C_{light}(V_{sat}) - C_{dark}(V_{sat})] \times \Delta V, \quad (22)$$

where $\Delta V = V_0 - V_{sat}$, and where V_0 is the built-in voltage.⁴³ This saturated capacitance ($C_{sat} = C_{light} - C_{dark}$) should not be confused with the geometric capacitance C_g discussed in detail in Sec. II B.⁸³

There exist more complex approaches that use an iterative process to calculate the saturated charge carrier density n_{sat} .⁷³ However, as shown in the literature, how and whether n_{sat} is calculated at all usually is of less importance for the investigation of solar cell properties in the forward bias regime, specifically if high performing systems are chosen. This is the case, because the chemical capacitance C_{μ} and the excess charge carrier density n_{exc} are significantly larger in relation to the saturated capacitance C_{sat} and the saturated charge carrier density n_{sat} for high performing devices.⁸³ Thus, the

total charge carrier density and excess charge carrier density can be assumed to be approximately equal ($n_{\text{tot}} \approx n_{\text{exc}}$) most of the time, as is the case in the current example of a PM6:Y6 device. Nonetheless, the role of the saturated charge carrier density n_{sat} has been mentioned here for completeness.

C. Direct comparison of techniques

The different techniques discussed in this Tutorial, namely, TPV/TPC, IS, and CS, were applied to the same solar cells in an effort to gauge whether there are any significant differences in the subsequently determined charge carrier densities (cf. Fig. 13). A PM6:Y6 solar cell ($PCE = 14.7\%$) representing high performing devices and a P3HT:PCBM solar cell ($PCE = 4.2\%$) representing low performing devices were compared. In particular, the PM6:Y6 solar cell was studied via TPV/TPC (based on the data in Fig. 4), IS (based on the data in Fig. 9), and CS (based on the data in Fig. 11), whereas a comparison between TPV/TPC and IS for a P3HT:PCBM solar cell at open-circuit conditions was carried out in a previous study by Nakano *et al.*⁴⁷ The main results of this study are highlighted here as well. As can be seen, TPV/TPC, IS, and CS yield comparable results for the charge carrier density at open-circuit conditions for different light intensities. However, the IS/CS technique results in more data points beyond open-circuit conditions, which cannot be obtained via TPV/TPC, thus offering more insight with regard to the properties of the devices.

Additionally, experimental methods such as CE and BACE (cf. Sec. I) as well as computational approaches such as drift-diffusion simulations could be used as further verification. However, this is beyond the scope of the present Tutorial.

V. CONCLUSIONS

In conclusion, different types of differential charging measurement techniques, namely, TPV/TPC, IS, and CS, have been explored in detail with regard to their ability to determine the charge carrier density of organic solar cells. In general, both techniques rely on the measurement of the capacitance related to the presence of charge carriers in the investigated device, which can be obtained via an optical (TPV/TPC) or electrical (IS/CS) perturbation. The discussed approaches yield comparable values for the charge carrier density, as demonstrated for a high performing PM6:Y6 solar cell, which also replicates previous studies that performed a similar comparison for a P3HT:PCBM device. However, TPV/TPC is only limited to open-circuit conditions. Thus, other points of interest, such as short-circuit, maximum-power, or reverse bias, cannot be investigated with this technique. Also, parasitic effects or contributions from other layers cannot easily be modeled and corrected, although this should not have a significant effect in the investigation of high performing organic solar cells. On the other hand, TPV/TPC measurements have the advantage that they only rely on standard equipment that should be available in most optoelectronic laboratories, which makes it an ideal method for initial tests to determine the charge carrier density.

The other investigated approaches, namely, IS and CS, usually require dedicated equipment to obtain meaningful results. In addition, specifically the development of detailed equivalent circuit models and initial compensation measurements are necessary to

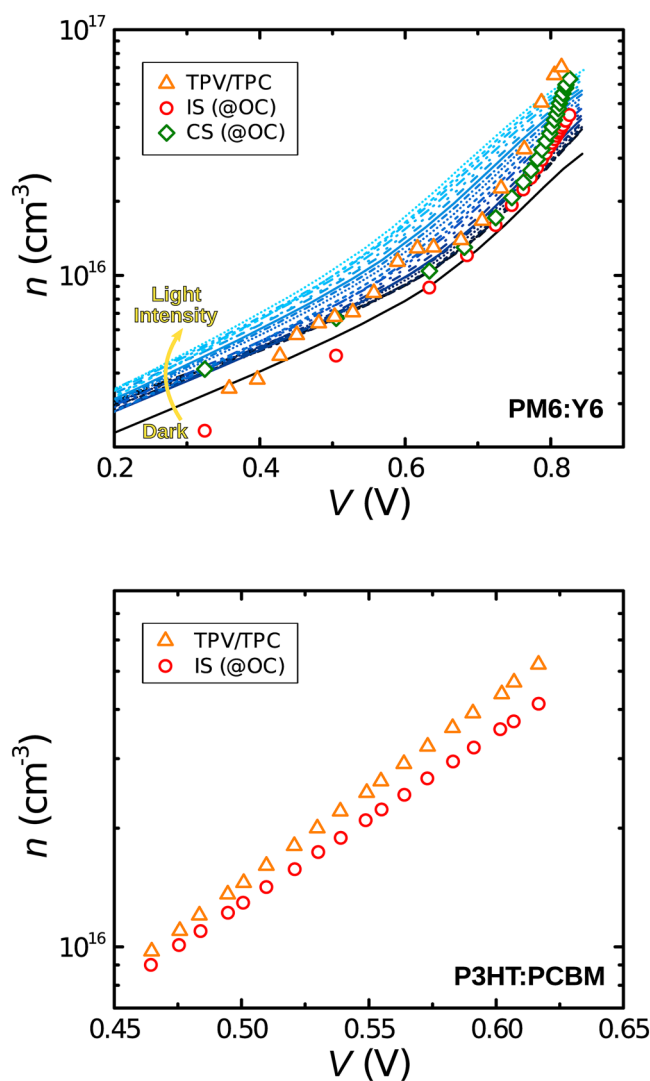


FIG. 13. Comparison of the charge carrier density n determined via TPV/TPC (orange triangles), IS (red circles under open-circuit), and CS (green diamonds under open-circuit) for a solar cell based on PM6:Y6 and P3HT:PCBM.⁴⁷ Charge carrier densities n determined via capacitance spectroscopy under other conditions than open-circuit are depicted by the blue colored lines for the PM6:Y6 device.

minimize the influence of parasitic effects and other contributing factors. In contrast to TPV/TPC, IS and CS offer more opportunities for a direct comparison with other, independent measurement results, such as in the case of the series resistance or shunt resistance. Furthermore, IS and CS can be performed at a multitude of applied biases, thus enabling the determination of the charge carrier density at open-circuit, short-circuit, maximum-power, and reverse bias. In addition, frequency-resolved measurements are possible, which can reveal more sophisticated aspects, such as the influence of trap states or the Maxwell displacement current capacitance of the depletion region. For instance, the combination of IS/CS with J - V -characteristics is a powerful tool, which can yield substantial insight with regard to the recombination and extraction dynamics of organic solar cells. However, great care is necessary when the fundamental IS/CS measurements are performed, otherwise parasitic effects, oversimplified models, or erroneous analyses can yield meaningless results and lead to false conclusions.

In summary, differential charging techniques are a great approach to quantify the charge carrier density of organic solar cells under realistic operating conditions. TPV/TPC can be categorized as the beginner friendly option, whereas IS/CS can yield more detailed results at the cost of specialized equipment and more complex data acquisition and analysis.

ACKNOWLEDGMENTS

This work has been funded by the Alexander-von-Humboldt Stiftung (Sofja-Kovalewskaja-Award). J.V. acknowledges funding by the Alexander-von-Humboldt Stiftung (Feodor-Lynen-Rückkehrstipendium) and by a Brückenstipendium of the University of Potsdam. V.V.B. acknowledges the Faculty-Development Competitive Research Program of Nazarbayev University (Grant No. 11022021FD2915).

AUTHOR DECLARATIONS

Conflict of Interest

The authors have no conflicts to disclose.

DATA AVAILABILITY

The data that support the findings of this study are available within the article.

APPENDIX A: DEVICE FABRICATION

The devices were fabricated on pre-etched ITO glass, following a routine cleaning procedure in Hellmanex, de-ionized water, acetone, and isopropyl alcohol. A 30 nm thick PEDOT:PSS film was spin-coated and annealed at 150 °C for 20 min in air to act as a hole-transporting layer. To obtain a PM6:Y6 solar cell, PM6 donor polymer was mixed with Y6 non-fullerene acceptor at the 1:1.2 weight ratio and dissolved in chloroform with 0.5% of chloronaphthalene. After spin-coating in a nitrogen glovebox, the sample with the approximate active layer thickness of 100 nm was annealed at 110 °C for 10 min. Prior to thermal evaporation of the Ag (100 nm) electrode, a 10 nm thick PDINO layer was spin-coated in nitrogen to act as an electron-transporting layer. After active layer

spin-coating in a nitrogen glovebox, a combination of LiF (0.8 nm) and Al (100 nm) was thermally evaporated to act as a cathode.

APPENDIX B: TRANSIENT PHOTOVOLTAGE AND PHOTOCURRENT MEASUREMENTS

The combined TPV/TPC measurements were performed using an EKSPLA NT242 pulsed laser (at 532 nm), white light background LED illumination, and an Agilent DSO9054H high-definition oscilloscope with an input impedance of 1 M Ω for TPV and 50 Ω for TPC measurements. To improve the TPV measurement, input impedance values as high as 1.5 T Ω have previously been used.⁸⁷

APPENDIX C: IMPEDANCE MEASUREMENTS

The impedance measurements were performed using a Keysight E5061B Vector Network Analyzer. Prior to the measurements, the tool was calibrated using a 85032E Type N calibration kit. This was followed by the tool compensation procedure using the “Open,” “Short,” and “50 Ω ” measurements at the device connection fixture. The measurements were performed in the frequency range from 50 Hz to 10 MHz. During the measurement, the devices were illuminated by a white-light LED array providing the required intensity.

REFERENCES

- ¹G. Yu, J. Gao, J. C. Hummelen, F. Wudl, and A. J. Heeger, “Polymer photovoltaic cells: Enhanced efficiencies via a network of internal donor-acceptor heterojunctions,” *Science* **270**, 1789–1791 (1995).
- ²Y.-J. Cheng, S.-H. Yang, and C.-S. Hsu, “Synthesis of conjugated polymers for organic solar cell applications,” *Chem. Rev.* **109**, 5868–5923 (2009).
- ³G. Li, R. Zhu, and Y. Yang, “Polymer solar cells,” *Nat. Photonics* **6**, 153–161 (2012).
- ⁴Y. Lin and X. Zhan, “Oligomer molecules for efficient organic photovoltaics,” *Acc. Chem. Res.* **49**, 175–183 (2016).
- ⁵L. Lu, T. Zheng, Q. Wu, A. M. Schneider, D. Zhao, and L. Yu, “Recent advances in bulk heterojunction polymer solar cells,” *Chem. Rev.* **115**, 12666–12731 (2015).
- ⁶S. B. Darling and F. You, “The case for organic photovoltaics,” *RSC Adv.* **3**, 17633–17648 (2013).
- ⁷J. Guo and J. Min, “A cost analysis of fully solution-processed ITO-free organic solar modules,” *Adv. Energy Mater.* **9**, 1802521 (2019).
- ⁸N. S. Sariciftci, “Polymeric photovoltaic materials,” *Curr. Opin. Solid State Mater. Sci.* **4**, 373–378 (1999).
- ⁹M. P. Hughes, K. D. Rosenthal, N. A. Ran, M. Seifrid, G. C. Bazan, and T.-Q. Nguyen, “Determining the dielectric constants of organic photovoltaic materials using impedance spectroscopy,” *Adv. Funct. Mater.* **28**, 1801542 (2018).
- ¹⁰J. Vollbrecht, J. Lee, S.-J. Ko, V. V. Brus, A. Karki, W. Le, M. Seifrid, M. J. Ford, K. Cho, G. C. Bazan *et al.*, “Design of narrow bandgap non-fullerene acceptors for photovoltaic applications and investigation of non-geminate recombination dynamics,” *J. Mater. Chem. C* **8**, 15175–15182 (2020).
- ¹¹Y. Lin, Y. Firdaus, F. H. Isikgor, M. I. Nugraha, E. Yengel, G. T. Harrison, R. Hallani, A. El-Labban, H. Faber, C. Ma *et al.*, “Self-assembled monolayer enables hole transport layer-free organic solar cells with 18% efficiency and improved operational stability,” *ACS Energy Lett.* **5**, 2935–2944 (2020).
- ¹²M. Zhang, L. Zhu, G. Zhou, T. Hao, C. Qiu, Z. Zhao, Q. Hu, B. W. Larson, H. Zhu, Z. Ma *et al.*, “Single-layered organic photovoltaics with

double cascading charge transport pathways: 18% efficiencies,” *Nat. Commun.* **12**, 1–10 (2021).

¹³Y. Cui, Y. Xu, H. Yao, P. Bi, L. Hong, J. Zhang, Y. Zu, T. Zhang, J. Qin, J. Ren *et al.*, “Single-junction organic photovoltaic cell with 19% efficiency,” *Adv. Mater.* **33**, 2102420 (2021).

¹⁴Y. Lin, J. Wang, Z.-G. Zhang, H. Bai, Y. Li, D. Zhu, and X. Zhan, “An electron acceptor challenging fullerenes for efficient polymer solar cells,” *Adv. Mater.* **27**, 1170–1174 (2015).

¹⁵C. B. Nielsen, S. Holliday, H.-Y. Chen, S. J. Cryer, and I. McCulloch, “Non-fullerene electron acceptors for use in organic solar cells,” *Acc. Chem. Res.* **48**, 2803–2812 (2015).

¹⁶A. Kuzmich, D. Padula, H. Ma, and A. Troisi, “Trends in the electronic and geometric structure of non-fullerene based acceptors for organic solar cells,” *Energy Environ. Sci.* **10**, 395–401 (2017).

¹⁷G. Zhang, J. Zhao, P. C. Chow, K. Jiang, J. Zhang, Z. Zhu, J. Zhang, F. Huang, and H. Yan, “Nonfullerene acceptor molecules for bulk heterojunction organic solar cells,” *Chem. Rev.* **118**, 3447–3507 (2018).

¹⁸J. Hou, O. Inganäs, R. H. Friend, and F. Gao, “Organic solar cells based on non-fullerene acceptors,” *Nat. Mater.* **17**, 119–128 (2018).

¹⁹Y. Xu, H. Yao, L. Ma, J. Wang, and J. Hou, “Efficient charge generation at low energy losses in organic solar cells: A key issues review,” *Rep. Prog. Phys.* **83**, 082601 (2020).

²⁰J. Lee, S.-J. Ko, H. Lee, J. Huang, Z. Zhu, M. Seifrid, J. Vollbrecht, V. V. Brus, A. Karki, H. Wang *et al.*, “Side-chain engineering of nonfullerene acceptors for near-infrared organic photodetectors and photovoltaics,” *ACS Energy Lett.* **4**, 1401–1409 (2019).

²¹R. Ma, T. Liu, Z. Luo, Q. Guo, Y. Xiao, Y. Chen, X. Li, S. Luo, X. Lu, M. Zhang *et al.*, “Improving open-circuit voltage by a chlorinated polymer donor endows binary organic solar cells efficiencies over 17%,” *Sci. China: Chem.* **63**, 325–330 (2020).

²²Q. Ma, Z. Jia, L. Meng, J. Zhang, H. Zhang, W. Huang, J. Yuan, F. Gao, Y. Wan, Z. Zhang *et al.*, “Promoting charge separation resulting in ternary organic solar cells efficiency over 17.5%,” *Nano Energy* **78**, 105272 (2020).

²³Y. Cui, H. Yao, L. Hong, T. Zhang, Y. Tang, B. Lin, K. Xian, B. Gao, C. An, P. Bi *et al.*, “Organic photovoltaic cell with 17% efficiency and superior processability,” *Natl. Sci. Rev.* **7**, 1239–1246 (2020).

²⁴A. Karki, J. Vollbrecht, A. J. Gillett, P. Selter, J. Lee, Z. Peng, N. Schopp, A. L. Dixon, M. Schrock, V. Nádaždy *et al.*, “Unifying charge generation, recombination, and extraction in low-offset non-fullerene acceptor organic solar cells,” *Adv. Energy Mater.* **10**, 2001203 (2020).

²⁵J. Yuan, Y. Zhang, L. Zhou, G. Zhang, H.-L. Yip, T.-K. Lau, X. Lu, C. Zhu, H. Peng, P. A. Johnson *et al.*, “Single-junction organic solar cell with over 15% efficiency using fused-ring acceptor with electron-deficient core,” *Joule* **3**, 1140–1151 (2019).

²⁶A. Karki, J. Vollbrecht, A. L. Dixon, N. Schopp, M. Schrock, G. M. Reddy, and T.-Q. Nguyen, “Understanding the high performance of over 15% efficiency in single-junction bulk heterojunction organic solar cells,” *Adv. Mater.* **31**, 1903868 (2019).

²⁷A. Karki, J. Vollbrecht, A. J. Gillett, S. S. Xiao, Y. Yang, Z. Peng, N. Schopp, A. L. Dixon, S. Yoon, M. Schrock *et al.*, “The role of bulk and interfacial morphology in charge generation, recombination, and extraction in non-fullerene acceptor organic solar cells,” *Energy Environ. Sci.* **13**, 3679–3692 (2020).

²⁸S. R. Cowan, N. Banerji, W. L. Leong, and A. J. Heeger, “Charge formation, recombination, and sweep-out dynamics in organic solar cells,” *Adv. Funct. Mater.* **22**, 1116–1128 (2012).

²⁹D. Credgington, F. C. Jamieson, B. Walker, T.-Q. Nguyen, and J. R. Durrant, “Quantification of geminate and non-geminate recombination losses within a solution-processed small-molecule bulk heterojunction solar cell,” *Adv. Mater.* **24**, 2135–2141 (2012).

³⁰W. Shockley and W. Read, Jr., “Statistics of the recombinations of holes and electrons,” *Phys. Rev.* **87**, 835 (1952).

³¹L. Koster, V. Mihailescu, and P. Blom, “Bimolecular recombination in polymer/fullerene bulk heterojunction solar cells,” *Appl. Phys. Lett.* **88**, 052104 (2006).

³²V. V. Brus, F. Lang, J. Bundesmann, S. Seidel, A. Denker, B. Rech, G. Landi, H. C. Neitzert, J. Rappich, and N. H. Nickel, “Defect dynamics in proton irradiated CH₃NH₃PbI₃ perovskite solar cells,” *Adv. Electron. Mater.* **3**, 1600438 (2017).

³³C. Göhler, A. Wagenpfahl, and C. Deibel, “Nongeminate recombination in organic solar cells,” *Adv. Electron. Mater.* **4**, 1700505 (2018).

³⁴V. V. Brus, “Light dependent open-circuit voltage of organic bulk heterojunction solar cells in the presence of surface recombination,” *Org. Electron.* **29**, 1–6 (2016).

³⁵J. Vollbrecht and V. V. Brus, “On the recombination order of surface recombination under open circuit conditions,” *Org. Electron.* **86**, 105905 (2020).

³⁶J. Vollbrecht and V. V. Brus, “Effects of recombination order on open-circuit voltage decay measurements of organic and perovskite solar cells,” *Energies* **14**, 4800 (2021).

³⁷C. Shuttle, A. Maurano, R. Hamilton, B. O’regan, J. C. de Mello, and J. Durrant, “Charge extraction analysis of charge carrier densities in a polythiophene/fullerene solar cell: Analysis of the origin of the device dark current,” *Appl. Phys. Lett.* **93**, 183501 (2008).

³⁸J. W. Ryan and E. Palomares, “Photo-induced charge carrier recombination kinetics in small molecule organic solar cells and the influence of film nanomorphology,” *Adv. Energy Mater.* **7**, 1601509 (2017).

³⁹J. Knipert, I. Lange, J. Heidbrink, J. Kurpiers, T. J. K. Brenner, L. J. A. Koster, and D. Neher, “Effect of solvent additive on generation, recombination, and extraction in PTB7:PCBM solar cells: A conclusive experimental and numerical simulation study,” *J. Phys. Chem. C* **119**, 8310–8320 (2015).

⁴⁰D. Credgington, Y. Kim, J. Labram, T. D. Anthopoulos, and J. R. Durrant, “Analysis of recombination losses in a pentacene/C₆₀ organic bilayer solar cell,” *J. Phys. Chem. Lett.* **2**, 2759–2763 (2011).

⁴¹D. Kiermasch, A. Baumann, M. Fischer, V. Dyakonov, and K. Tvingstedt, “Revisiting lifetimes from transient electrical characterization of thin film solar cells; a capacitive concern evaluated for silicon, organic and perovskite devices,” *Energy Environ. Sci.* **11**, 629–640 (2018).

⁴²J. Bisquert, “Chemical capacitance of nanostructured semiconductors: Its origin and significance for nanocomposite solar cells,” *Phys. Chem. Chem. Phys.* **5**, 5360–5364 (2003).

⁴³C. M. Proctor, C. Kim, D. Neher, and T.-Q. Nguyen, “Nongeminate recombination and charge transport limitations in diketopyrrolopyrrole-based solution-processed small molecule solar cells,” *Adv. Funct. Mater.* **23**, 3584–3594 (2013).

⁴⁴T. Kirchartz, W. Gong, S. A. Hawks, T. Agostinelli, R. C. I. MacKenzie, Y. Yang, and J. Nelson, “Sensitivity of the Mott–Schottky analysis in organic solar cells,” *J. Phys. Chem. C* **116**, 7672–7680 (2012).

⁴⁵N. Schopp, V. V. Brus, J. Lee, A. Dixon, A. Karki, T. Liu, Z. Peng, K. R. Graham, H. Ade, G. C. Bazan *et al.*, “Effect of palladium-tetrakis (triphenylphosphine) catalyst traces on charge recombination and extraction in non-fullerene-based organic solar cells,” *Adv. Funct. Mater.* **31**, 2009363 (2021).

⁴⁶R. A. Awni, Z. Song, C. Chen, C. Li, C. Wang, M. A. Razooqi, L. Chen, X. Wang, R. J. Ellingson, J. V. Li, and Y. Yan, “Influence of charge transport layers on capacitance measured in halide perovskite solar cells,” *Joule* **4**, 644–657 (2020).

⁴⁷K. Nakano, Y. Chen, and K. Tajima, “Quantifying charge carrier density in organic solar cells by differential charging techniques,” *AIP Adv.* **9**, 125205 (2019).

⁴⁸A. Maurano, C. G. Shuttle, R. Hamilton, A. M. Ballantyne, J. Nelson, W. Zhang, M. Heeney, and J. R. Durrant, “Transient optoelectronic analysis of charge carrier losses in a selenophene/fullerene blend solar cell,” *J. Phys. Chem. C* **115**, 5947–5957 (2011).

⁴⁹C. R. McNeill, I. Hwang, and N. C. Greenham, “Photocurrent transients in all-polymer solar cells: Trapping and detrapping effects,” *J. Appl. Phys.* **106**, 024507 (2009).

⁵⁰R. C. MacKenzie, C. G. Shuttle, M. L. Chabiny, and J. Nelson, “Extracting microscopic device parameters from transient photocurrent measurements of P3HT:PCBM solar cells,” *Adv. Energy Mater.* **2**, 662–669 (2012).

⁵¹D. Credgington, S.-W. Liu, J. Nelson, and J. R. Durrant, “*In situ* measurement of energy level shifts and recombination rates in subphthalocyanine/C₆₀ bilayer solar cells,” *J. Phys. Chem. C* **118**, 22858–22864 (2014).

- ⁵²J.-M. Nunzi, "Organic materials and devices for photovoltaic applications," in *Photovoltaic and Photoactive Materials—Properties, Technology and Applications*, edited by J. M. Marshall and D. Dimova-Malinovska (Springer Netherlands, Dordrecht, 2002), pp. 197–224.
- ⁵³G. D. Pozo, B. Romero, and B. Arredondo, *Proc. SPIE* **8435**, 84351Z (2012).
- ⁵⁴V. V. Brus, C. M. Proctor, N. A. Ran, and T.-Q. Nguyen, "Capacitance spectroscopy for quantifying recombination losses in nonfullerene small-molecule bulk heterojunction solar cells," *Adv. Energy Mater.* **6**, 1502250 (2016).
- ⁵⁵M. Horibe, "Performance comparisons between impedance analyzers and vector network analyzers for impedance measurement below 100 mHz frequency," in *2017 89th ARFTG Microwave Measurement Conference (ARFTG)* (IEEE, 2017), pp. 1–4.
- ⁵⁶D. Aurbach, M. D. Levi, E. Levi, H. Teller, B. Markovsky, G. Salitra, U. Heider, and L. Heider, "Common electroanalytical behavior of Li intercalation processes into graphite and transition metal oxides," *J. Electrochem. Soc.* **145**, 3024 (1998).
- ⁵⁷E. Von Hauff, "Impedance spectroscopy for emerging photovoltaics," *J. Phys. Chem. C* **123**, 11329–11346 (2019).
- ⁵⁸Q. Wang, J.-E. Moser, and M. Grätzel, "Electrochemical impedance spectroscopic analysis of dye-sensitized solar cells," *J. Phys. Chem. B* **109**, 14945–14953 (2005).
- ⁵⁹J.-B. Jorcin, M. E. Orazem, N. Pébère, and B. Tribollet, "CPE analysis by local electrochemical impedance spectroscopy," *Electrochim. Acta* **51**, 1473–1479 (2006).
- ⁶⁰T. Springer, T. Zawodzinski, M. Wilson, and S. Gottesfeld, "Characterization of polymer electrolyte fuel cells using AC impedance spectroscopy," *J. Electrochem. Soc.* **143**, 587 (1996).
- ⁶¹N. Kuriyama, T. Sakai, H. Miyamura, I. Uehara, H. Ishikawa, and T. Iwasaki, "Electrochemical impedance and deterioration behavior of metal hydride electrodes," *J. Alloys Compd.* **202**, 183–197 (1993).
- ⁶²Z. Deng, Z. Zhang, Y. Lai, J. Liu, J. Li, and Y. Liu, "Electrochemical impedance spectroscopy study of a lithium/sulfur battery: Modeling and analysis of capacity fading," *J. Electrochem. Soc.* **160**, A553 (2013).
- ⁶³A. S. Baranski and A. Szulborska, "High frequency impedance measurements at ultramicroelectrodes," *Electrochim. Acta* **41**, 985–991 (1996).
- ⁶⁴J. Vollbrecht, V. V. Brus, S.-J. Ko, J. Lee, A. Karki, D. X. Cao, K. Cho, G. C. Bazan, and T.-Q. Nguyen, "Quantifying the nongeminate recombination dynamics in nonfullerene bulk heterojunction organic solar cells," *Adv. Energy Mater.* **9**, 1901438 (2019).
- ⁶⁵V. V. Brus, N. Schopp, S.-J. Ko, J. Vollbrecht, J. Lee, A. Karki, G. C. Bazan, and T.-Q. Nguyen, "Temperature and light modulated open-circuit voltage in nonfullerene organic solar cells with different effective bandgaps," *Adv. Energy Mater.* **11**, 2003091 (2021).
- ⁶⁶D. Kiermasch, L. Gil-Escrig, H. J. Bolink, and K. Tvingstedt, "Effects of masking on open-circuit voltage and fill factor in solar cells," *Joule* **3**, 16–26 (2019).
- ⁶⁷V. Brus, "On impedance spectroscopy analysis of nonideal heterojunctions," *Semicond. Sci. Technol.* **27**, 035024 (2012).
- ⁶⁸J. Bisquert, L. Bertoluzzi, I. Mora-Sero, and G. Garcia-Belmonte, "Theory of impedance and capacitance spectroscopy of solar cells with dielectric relaxation, drift-diffusion transport, and recombination," *J. Phys. Chem. C* **118**, 18983–18991 (2014).
- ⁶⁹J. I. Basham, T. N. Jackson, and D. J. Gundlach, "Predicting the J-V curve in organic photovoltaics using impedance spectroscopy," *Adv. Energy Mater.* **4**, 1400499 (2014).
- ⁷⁰B. Ecker, H.-J. Egelhaaf, R. Steim, J. Parisi, and E. von Hauff, "Understanding S-shaped current-voltage characteristics in organic solar cells containing a TiO_x interlayer with impedance spectroscopy and equivalent circuit analysis," *J. Phys. Chem. C* **116**, 16333–16337 (2012).
- ⁷¹J. Vollbrecht, C. Wiebeler, H. Bock, S. Schumacher, and H.-S. Kitzerow, "Curved polar dibenzocoronene esters and imides versus their planar centrosymmetric homologs: Photophysical and optoelectronic analysis," *J. Phys. Chem. C* **123**, 4483–4492 (2019).
- ⁷²A. Guerrero, L. F. Marchesi, P. P. Boix, J. Bisquert, and G. Garcia-Belmonte, "Recombination in organic bulk heterojunction solar cells: Small dependence of interfacial charge transfer kinetics on fullerene affinity," *J. Phys. Chem. Lett.* **3**, 1386–1392 (2012).
- ⁷³M. C. Heiber, T. Okubo, S.-J. Ko, B. R. Luginbuhl, N. A. Ran, M. Wang, H. Wang, M. A. Uddin, H. Y. Woo, G. C. Bazan *et al.*, "Measuring the competition between bimolecular charge recombination and charge transport in organic solar cells under operating conditions," *Energy Environ. Sci.* **11**, 3019–3032 (2018).
- ⁷⁴N. Tokmoldin, J. Vollbrecht, S. M. Hosseini, B. Sun, L. Perdígón-Toro, H. Y. Woo, Y. Zou, D. Neher, and S. Shoaee, "Explaining the fill-factor and photocurrent losses of nonfullerene acceptor-based solar cells by probing the long-range charge carrier diffusion and drift lengths," *Adv. Energy Mater.* **11**, 2100804 (2021).
- ⁷⁵T. Walter, R. Herberholz, C. Müller, and H. Schock, "Determination of defect distributions from admittance measurements and application to Cu(In,Ga)Se₂ based heterojunctions," *J. Appl. Phys.* **80**, 4411–4420 (1996).
- ⁷⁶J. Fischer, D. Ray, H. Kleemann, P. Pahnner, M. Schwarze, C. Koerner, K. Vandewal, and K. Leo, "Density of states determination in organic donor-acceptor blend layers enabled by molecular doping," *J. Appl. Phys.* **117**, 245501 (2015).
- ⁷⁷G. Garcia-Belmonte, P. P. Boix, J. Bisquert, M. Sessolo, and H. J. Bolink, "Simultaneous determination of carrier lifetime and electron density-of-states in P3HT:PCBM organic solar cells under illumination by impedance spectroscopy," *Sol. Energy Mater. Sol. Cells* **94**, 366–375 (2010).
- ⁷⁸J. Bisquert, I. Mora-Sero, and F. Fabregat-Santiago, "Diffusion-recombination impedance model for solar cells with disorder and nonlinear recombination," *ChemElectroChem* **1**, 289–296 (2013).
- ⁷⁹A. K. Jonscher, "The physical origin of negative capacitance," *J. Chem. Soc., Faraday Trans. 2* **82**, 75–81 (1986).
- ⁸⁰M. Ershov, H. Liu, L. Li, M. Buchanan, Z. Wasilewski, and A. K. Jonscher, "Negative capacitance effect in semiconductor devices," *IEEE Trans. Electron Devices* **45**, 2196–2206 (1998).
- ⁸¹E. Ehrenfreund, C. Lungenschmied, G. Dennler, H. Neugebauer, and N. Sariciftci, "Negative capacitance in organic semiconductor devices: Bipolar injection and charge recombination mechanism," *Appl. Phys. Lett.* **91**, 012112 (2007).
- ⁸²Q. Niu, N. I. Crăciun, G.-J. A. Wetzelaer, and P. W. Blom, "Origin of negative capacitance in bipolar organic diodes," *Phys. Rev. Lett.* **120**, 116602 (2018).
- ⁸³J. Vollbrecht and V. V. Brus, "On charge carrier density in organic solar cells obtained via capacitance spectroscopy," *Adv. Electron. Mater.* **6**, 2000517 (2020).
- ⁸⁴L. Xu, J. Wang, and J. W. Hsu, "Transport effects on capacitance-frequency analysis for defect characterization in organic photovoltaic devices," *Phys. Rev. Appl.* **6**, 064020 (2016).
- ⁸⁵M. Azzouzi, P. Calado, A. M. Telford, F. Eisner, X. Hou, T. Kirchartz, P. R. Barnes, and J. Nelson, "Overcoming the limitations of transient photovoltage measurements for studying recombination in organic solar cells," *Sol. RRL* **4**, 1900581 (2020).
- ⁸⁶I. Zonno, H. Zayani, M. Grzeslo, B. Krogmeier, and T. Kirchartz, "Extracting recombination parameters from impedance measurements on organic solar cells," *Phys. Rev. Appl.* **11**, 054024 (2019).
- ⁸⁷A. Pockett, H. K. H. Lee, B. L. Coles, W. C. Tsoi, and M. J. Carnie, "A combined transient photovoltage and impedance spectroscopy approach for a comprehensive study of interlayer degradation in non-fullerene acceptor organic solar cells," *Nanoscale* **11**, 10872–10883 (2019).